**Title**

Fiber Adhesion and Interactions of Vessel Distribution and Density in the Impact Resistance of Wood

**Permalink**

https://escholarship.org/uc/item/6q86z67s

**Author**

Matsushita, Albert Keisuke

**Publication Date**

2017

Peer reviewed|Thesis/dissertation

UNIVERSITY OF CALIFORNIA, SAN DIEGO

# Fiber Adhesion and interactions of Vessel Distribution and Density in the Impact Resistance of Wood

A Thesis submitted in partial satisfaction of the requirements for the degree Master of Science

in

Materials Science and Engineering

by

Albert Keisuke Matsushita

Committee in Charge

Professor Joanna M. McKittrick, Chair
Professor Shengqiang Cai
Professor Marc Meyers

2017

The Thesis of Albert Keisuke Matsushita is approved and it is acceptable in quality and form for publication on microfilm and electronically:

Chair

University of California, San Diego

2017

# Table of Contents

# List of Figures

# List of Tables

# Acknowledgements

I would like to acknowledge Professor Joanna McKittrick for her support as the chair of my committee and for her trust in this exploratory work. In addition, I thank my committee members Professor Shengqiang Cai and Professor Marc Meyers for their critique and guidance.

I would also like to acknowledge the contributions of the following individuals: Meng Wang and Professor Yu Qiao for helping me perform drop-tower experiments on the CEAST 9350 (continuing to do so even after I broke their striker) and providing thoughtful insight on the failure modes observed in wood; Damian Gonzalez (University of California San Diego, 2015) and Jennifer Doan (University of California San Diego, 2019) for their invaluable contributions to the refinement of protocols, development of 3D models, and collection of data in imaging and drop-tower experiments; the Berdoll Sawmill Company of Austin, TX for their generous contribution of Southern Live Oak, and Thomas Chalfant and Ian Richardson for their wood working expertise and helping to prepare my samples. Finally I would like to thank all members of Professor McKittrick's research lab for their guidance, knowledge in experimental methods, and comradery.

This work has been made possible by the Multi-University Research Initiative through the Air Force Office of Scientific Research (AFOSR-FA9550-15-1-0009) and the the National Science Foundation's research grant on biomaterials (1507978).

# ABSTRACT OF THE THESIS

## Fiber Adhesion and Interactions of Vessel Distribution and Density in the Impact Resistance of Wood

by

Albert Keisuke Matsushita

Master of Science in Materials Science and Engineering

University of California, San Diego, 2017

Professor Joanna M. McKittrick, Chair

This thesis investigates the effects of wood anatomy on the low velocity dynamic impact response of wood species in radial-loading drop-tower testing. The distribution of vessel elements was found to significantly alter the normalized impact energy of failure: diffuse porous species (uniform vessel distribution) saw improved impact resistance with increasing density, while ring porous species (tangential bands of vessels in the growth stage of growth rings) did not. Unlike in quasi-static conditions density alone was not an accurate predictor of failure energy in impact. Examination of quasi-statically and dynamically damaged ring porous white ash revealed that while vessels collapsed and absorbed energy under slow loading, they became stress concentrators in impact. Radial dynamic loading caused crack propagation in the tangential direction, which in the ring porous distribution of vessels in tangential bands allowed successive breaking of vessels. In diffuse porous species the uniform distribution of vessels did not provide any crack path and therefore saw improvements in dynamic work to fracture with increased density. The dynamic load-time responses revealed higher amplitude oscillations in ring porous wood species near the initial moment of impact due to a combination of sequential vessel breaking and high fiber adhesion. Species able to maintain low peak forces exhibited failure mechanisms like progressive delamination observed in fiber-reinforced composites. Hierarchical deformation mechanisms were also observed such as tracheid unwinding in African mahogany and red alder. These findings may be used to inform bio-inspired impact resistant materials that incorporate porosity and hierarchical damage absorption structures.

# 1 Introduction

Millennia of evolution have honed biological materials into highly efficient structures for their specialized roles. Biological materials combine a wide variety of features including density gradients, hierarchical architectures, cellular configurations, layered composites, and more to maximize performance while minimizing mass (a penalty in terms of the energy and resources required to grow it and for the organism to remain mobile). Impact resistant biological materials are no exception as research continues to unlock the structural features behind their shock absorbent abilities [1]:

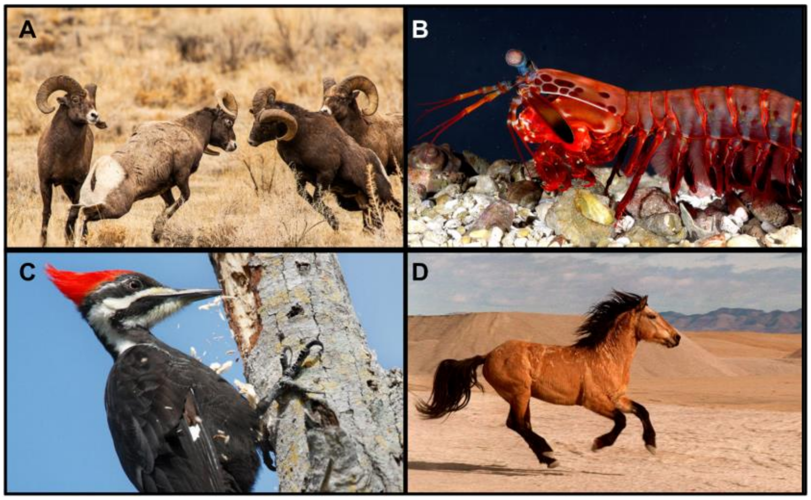

**Figure 1.** Animals with impact resistant structures. (A) Male Bighorn sheep compete for mating rites by butting heads without sustaining brain injury [2], (B) Mantis shrimp use their dactyl clubs to smash open the shells of clams, their prey [3], (C) Woodpeckers bore holes into trees using their beaks while avoiding brain injury[4], (D) Mongol horses gallop safely across the rough terrain of the Mongolian steppes [5]. Figures are adapted from cited sources.

Although a variety of animal biological materials have been investigated as shown in Figure 1, there is an entire class of biomaterials that has been neglected in the study of shock resistance:

wood. In everything from bowling alley flooring and baseball bats to gunstocks and the Aztec broadsword, woods such as Ash, Walnut, Maple, and others have long been used for their ability to bear dynamic loads [6]. Americans would be familiar with the wooden-hulled USS Constitution: a frigate that earned the moniker “Old Ironsides” after defeating several British ships in the War of 1812 and surviving barrages of cannon fire with little damage [7]. Through thousands of years worth of craftsmanship humans have determined several species of trees (Table 1) useful for impact resistant applications as shown in Figure 2—this work explores the structural features that these woods have in common that distinguish them from other species.

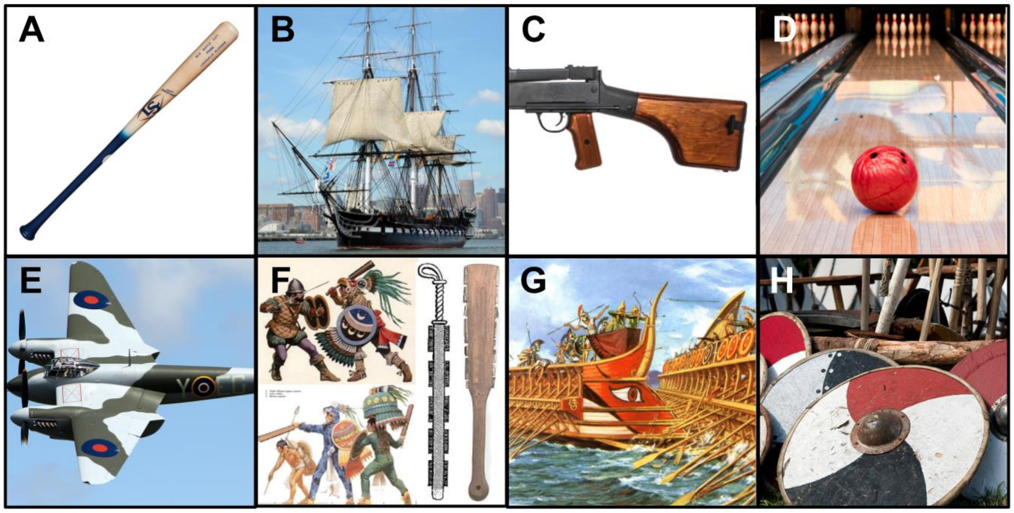

**Figure 2.** Various applications of impact resistant wood. (A) Louisville Slugger [8], (B) USS Constitution (“Old Ironsides”) [7], (C) Degtyaryov hand-held machine gun stock [9], (D) bowling alley flooring [10], (E) DH-98 Mosquito bomber [11], (F) Macuahuitl (Aztec broadsword) [12], (G) ancient Greek Trireme [13], and (H) Viking shields [14]. Figures are adapted from cited sources.

**Table 1.** Examples of impact resistant wood species, their uses, and mechanical properties (at 12% moisture content)

| **Wood Species** | **Uses** | **Fracture toughness (kPa$\sqrt{\text{m}}$)** | **Work to Maximum Load (kJ m$^{-3}$)** | **E(GPa)** | **$\sigma_y$ (MPa)** | **References** |
|---|---|---|---|---|---|---|
| *Black Walnut* | Furniture, gunstocks | | 74 | $^{T}$ 11.6 (b) | $^{T}$7 (c)<br>$^{L}$52 (c) | [6], [15] |
| *Black Willow* | Cricket bats, flooring, prosthetic limbs | | 71 | $^{T}$ 7 (b) | $^{T}$3 (c)<br>$^{L}$28 (c) | [6], [15] |
| *Boxwood* | Furniture, musical instruments, sports equipment | | | | | [6] |
| *Sugar Maple* | Baseball bats, bowling alleys, flooring | 480 (Mode I, TL, 3pt. bend) | 114 | $^{T}$ 12.6 (b) | $^{T}$10 (c)<br>$^{L}$54 (c) | [6], [15] |
| *Southern Live Oak* | Aztec broadsword (Fig. 2e), USS Constitution | | 130 | $^{T}$ 13.7 (b) | $^{T}$20 (c)<br>$^{L}$61 (c) | [15] |
| *White Ash* | Baseball bats, oars, tool handles | 790 (Mode I, TL, 3pt. bend) | 115 | $^{T}$ 12 (b) | $^{T}$8 (c)<br>$^{L}$51 (c) | [6], [15], [16] |

(b) = beam bending test results, (c) = compression test results, $^{T}$ = transverse direction, $^{L}$ = longitudinal direction

# 2 Background

## 2.1 The composition and structure of wood

Wood is a cellular solid characterized by three microstructural features: tracheids and fibers, rays, and vessels (Figure 3). Tracheids and fibers describe the long, axially growing cells comprising the bulk of gymnospermous (e.g. conifers, ginkgo, & cycads.) and angiospermous (flowering) trees, respectively. Many refer to these two groups of trees simply as softwoods and hardwoods, but these terms are misnomers having little to do with the mechanical properties of the trees (cork is technically a hardwood, for example). Rays are rectangular, radial arrays of cells responsible for the transport of nutrients and fluids from the center of a tree to the periphery, where tree growth occurs. Vessels provide a similar function in that they conduct fluids up a tree through their enlarged, thin walled pores, but are found only in angiosperms. In general, the microstructure of gymnosperms is simpler and consists almost entirely of tracheids while angiosperms exhibit greater diversity (Table 2). The microstructures of trees vary greatly from species to species but retain these three characteristics [6].

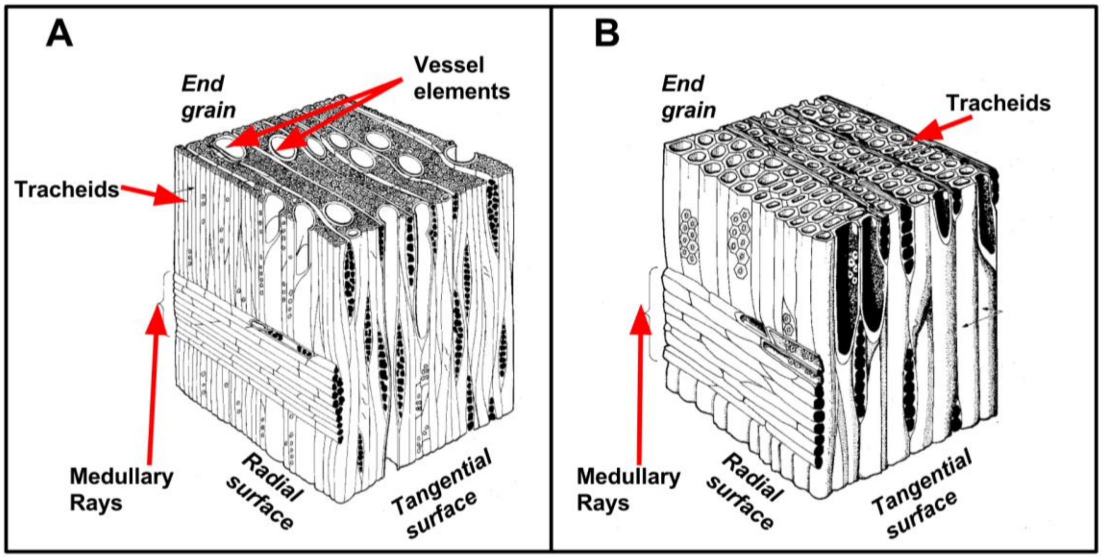

**Figure 3.** At a macroscopic level, wood is a closed foam cellular solid comprising tracheids, rays, and vessels. Tracheids are the long, narrow cells that make up the bulk of the wood and bear load. Rays are similarly shaped, radial arrays of cells responsible for the transport of nutrients and fluids from the center of a tree to the periphery. Vessels are large, thin walled tubules responsible for conducting fluids vertically. While (A) angiosperms (flowering trees, “hardwoods”) exhibit tracheids, rays, and vessels, (B) gymnosperms (conifers, “softwoods”) exhibit only tracheids and rays [17], [18]. Figures are adapted from cited sources.

**Table 2.** Cell type and makeup of gymnosperms (conifers, ginkgo, etc.) and angiosperms (flowering trees) [6].

| **Property** | **Gymnosperms** | | **Angiosperms** | | |
|---|---|---|---|---|---|
| | Tracheids | Rays | Tracheids | Rays | Vessels |
| *Volume fraction (%)* | 85-90 | 5-12 | 37-70 | 6-55 | 10-32 |
| *Axial dimension (mm)* | 2.5-7.0 | | 0.6-2.3 | 0.2-1.3 | |
| *Tangential dimension (μm)* | 25-80 | | 10-30 | 20-500 | |
| *Radial dimension (μm)* | 17-60 | | 10-30 | 20-350 | |
| *Cell wall thickness (μm)* | 2-7 | | 1-11 | | |

Figure 4 illustrates some of the anatomical diversity of angiosperms. Leopardwood (Figure 4, A) for example shows prominent aggregates of ray cells visible to the naked eye. White ash (Figure 4, B) shows vessels confined to tangential bands in an arrangement called ring porous vessel distribution. Sugar maple (Figure 4, C) shows a uniform distribution of smaller pores, called a diffuse porous vessel distribution. In ring porous trees the vessels only form during rapid spring and summer growth when resources are plentiful whereas in diffuse porous trees vessels grow throughout the seasons. Bitternut hickory (Figure 4, D) has vessels that grow in tangential bands but also decrease in size between the warm growth seasons and colder seasons (a pattern called semi-diffuse porous vessel distribution).

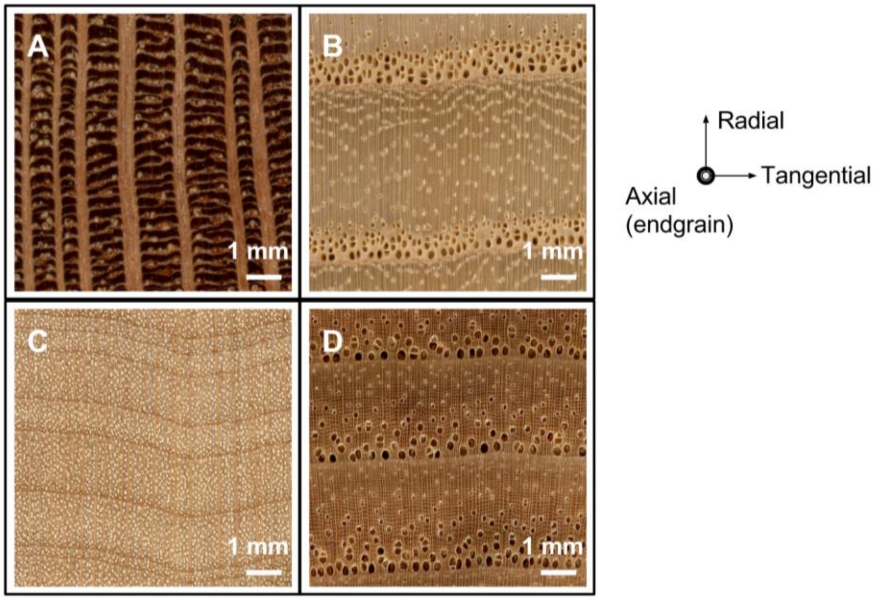

**Figure 4.** All wood features tracheids, rays, and vessels (Figure 3) in different proportions and arrangements as shown in the images of the axial faces (end grain) of these woods: (A) leopardwood[19] , (B) white ash [20], (C) sugar maple [21], (D) bitternut hickory [22]. Figures are adapted from cited sources.

The material forming the tracheid, ray, and vessel walls is a composite of semi-crystalline cellulose fibers $(C_6H_{10}O_5)_n$ embedded within an amorphous matrix of highly branched pectin $(C_6H_{10}O_7)_n$ or lignin $(C_{31}H_{34}O_{11})_n$. polysaccharides. The matrix composition depends on the stage of growth of the cell: young cell walls tend to be composed of pectin whereas older, lignified cell walls are composed of mostly lignin. The cellulose polysaccharides are arranged as macromolecular fibrils providing high tensile strength and are bound to the compression resistant matrix by smaller, branched hemicellulose $(C_{31}H_{34}O_{11})_n$. (As wood tissue matures, the matrix is increasingly reinforced by the highly cross-linked lignin. The matrix composition and cellulose fibril arrangement depend on the cell wall layer: from outermost to innermost they are the middle lamella (ML), primary (P), secondary 1 (S1), S2, and S3 wall, shown in Figure 5. The ML is the lignin rich layer of the cell wall responsible for binding neighboring cells. The P wall interior to the ML is thin and difficult to distinguish from the ML, but is characterized by randomly oriented cellulose microfibrils embedded in a pectin matrix. The subsequent S1 layer in contrast is made of cellulose microfibrils aligned in a helical fashion at a large angle of 50° to 70° between the direction of tree growth. The S2 layer also contains aligned microfibrils 0° to 45° to the longitudinal direction, but is far thicker (accounting for 80-90% of a tracheid’s mass) and bears most of the load on the tracheid. The final S3 layer contains microfibrils aligned >70° to the longitudinal direction and is thin with the lowest lignin content of all layers [23], [24]. Key characteristics of each layer are summarized in the cell wall layer properties of Table 3.

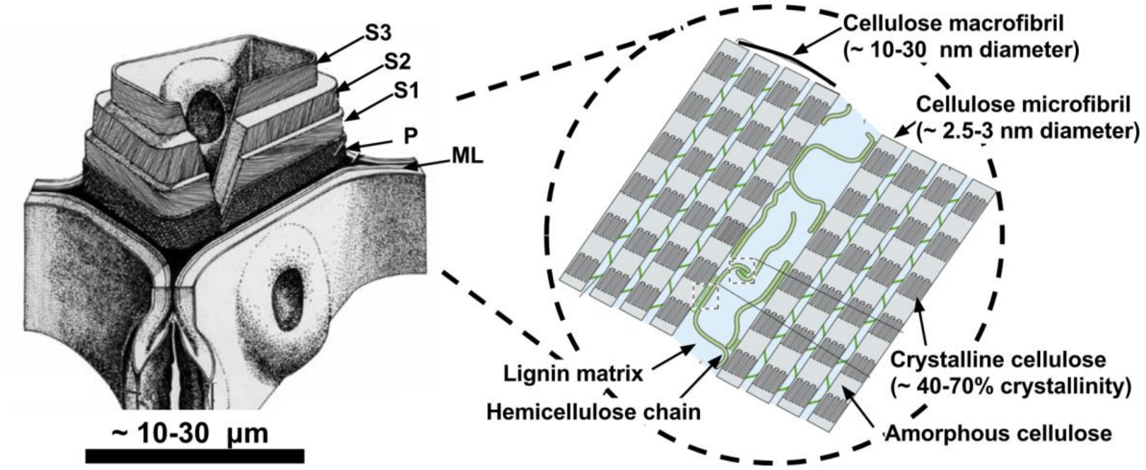

**Figure 5.** A composite of semi-crystalline cellulose fibers embedded in highly branched pectin or lignin polysaccharides forms the cell walls of wood, here illustrated in a tracheid. The organization depends on the layer of the cell wall (see Table 3). From outermost to innermost, they are the middle lamella (ML), primary (P), secondary 1 (S1), S2, and S3 wall [24], [25]. Figures are adapted from cited sources.

**Table 3.** Cell wall layer properties [26], [27]

| **Cell wall layer (outer to innermost)** | **Relative thickness (%)** | **Average microfibril angle to vertical axis** | **Cellulose content (w.t. %)** | **Hemicellulose content (w.t. %)** | **Lignin content (w.t. % )** |
|---|---|---|---|---|---|
| *Middle Lamella & Primary wall* | >1 | Random | 16 | 29 | 55 |
| *S1* | 10-22 | 50-70 | 44.6 | 33.4 | 22 |
| *S2* | 70-90 | 10-20 | 50.4 | 27.8 | 22 |
| *S3* | 2-8 | 60-90 | 43.8 | 34.2 | 22 |

Combining these many layers yields a stiff and tough cell wall (Table 4).
For comparison, spider silk (1300 kg/m$^3$) has a stiffness of 10 GPa and tensile strength of 600 MPa [28]. Bighorn sheep horn (1200 kg/m$^3$) has a stiffness of 2.2 GPa (at 10.6% moisture content) and compressive strength of 127 MPa [29]. Al 6061-T (2700 kg/m$^3$), commonly used in aircraft frames, has a stiffness of 68.9 GPa and tensile strength of 55 MPa [30].

**Table 4.** Cell wall mechanical properties

| **Property** | **Literature Value** |
|---|---|
| *Density* $(kg/m^3)$ | 1500 [31] |
| $E_{Axial}$ $(GPa)$ | 35 [32] |
| $E_{Transverse}$ $(GPa)$ | 10-19 [6], [32] |
| $G_{A\text{-}R,\ R\text{-}T}$ $(GPa)$ | 2.6 [6] |
| $\sigma_{y,\ Axial}$ $(MPa)$ | 120-350 [6], [33] |
| $\sigma_{y,\ Transverse}$ $(MPa)$ | 50-135 [6], [33] |
| $\tau_y$ $(MPa)$ | 30 [6] |
| *Toughness* $_{Peeling\ mode}$ $(J/m^2)$ | 350 [6] |
| *Toughness* $_{Breaking\ mode}$ $(J/m^2)$ | 1650 [6] |
| *Fracture toughness* $_{Peeling\ mode}$ $(MN/m^{3/2})$ | 1.9 [6] |
| *Fracture toughness* $_{Breaking\ mode}$ $(MN/m^{3/2})$ | 4.1 [6] |

## 2.2 Wood mechanical properties

The use of wood stretches from the dawn of humanity to the modern era where the global, annual production of timber rivals that of steel at roughly $10^9$ tons. Most of that wood is used for structural applications and is therefore well studied in static loading conditions. Research on dynamic loading conditions remains sparse, however, as discussed in Section 2.2.3 [6].

### 2.2.1 The stress strain curve of wood and anisotropy

Although the mechanical properties of the cell wall were described in Section 2.1, it is the bulk properties of wood that merit their use in everything from buildings and ships to sporting goods and furniture. Wood combines stiffness, toughness, and weight efficiency as evident in the Ashby plots developed by Gibson and Ashby shown in Figure 6.

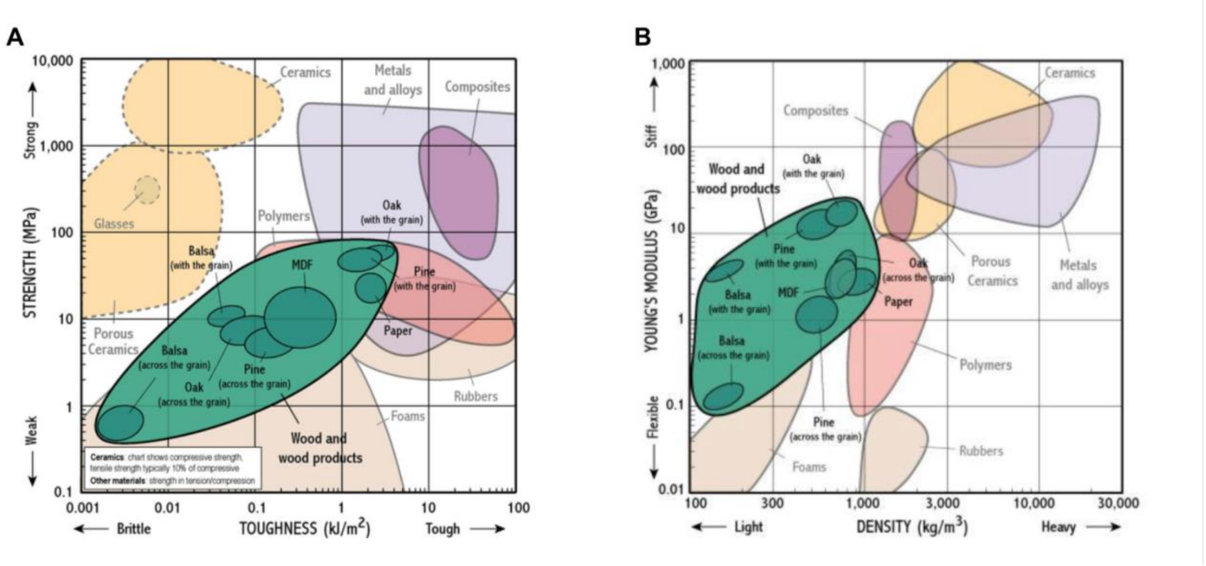

**Figure 6.** Ashby plots showcase (A) the strength and toughness of wood and (B) the weight efficiency of its stiffness relative to other materials. Figure adapted from [34].

The common commercial timber spruce, for example, has a stiffness of 30 GPa and yield strength of 300 MPa with a work of fracture between 15-30 kJ/m$^2$. In comparison aluminum has a Young's modulus of 69 GPa, yield strength of 500 MPa, and work of fracture of approximately 1000 kJ [24], [35]. The tradeoff is their weight-efficiency as seen in Figure 6, B: while spruce has a typical density of 450 kg/m$^3$, aluminum has a density of $\rho$ = 2700 kg/m$^3$, hence wood remains immensely useful in even modern structures. Another tradeoff is that unlike traditional engineering materials wood is highly anisotropic and exhibits unique stress strain behavior in each direction due to the elongated elements of its cellular structure. While tangential (T) and radial (R) loading produce similar results, axial (A) loading yields greater values of stiffness, strength, and other mechanical properties in general. The deformation mechanisms are also different: in tangential and radial compression the wood behaves linear elastically up to small strains (~.02) as the cell walls bend uniformly. Plastic yielding then propagates from the loading surface as the stress achieves a gently rising plateau. Once the cell walls fully densify the stress sharply increases until the wood fails. In axial loading the initial linear elastic regime is characterized by uniaxial cell compression instead of cell wall bending. Plastic yield occurs as the end caps joining the head-to-tail of neighboring cells fracture or the cell walls buckle in low density and high density woods, respectively. The collapse is visible as macroscopic bands of failed, crushed together cells. Eventually the wood densifies and the stress sharply increases as in radial and tangential loading [6]. Despite the differences in mechanisms between T, R, and A loading all three can be represented by the general three-region stress-strain curve in Figure 7. The linear elastic region is characterized by Young's modulus (E) and ends at the crushing or plateau stress ($\sigma_{pl}$), which proceeds to the densification strain ($\varepsilon_d$). The absorbed energy is calculated as the area under the curve (U).

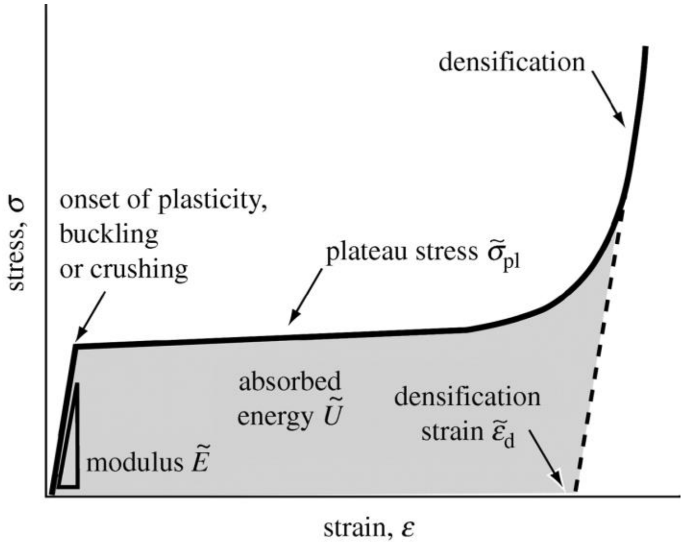

**Figure 7.** A typical stress-strain curve of wood in compression exhibits three distinct regions. Initially, the wood behaves linear elastically as the cell walls bend uniformly (in tangential and radial loading) or cells compress uniaxially (in axial loading) before yielding at ~0.02 strain. A plateau stress is then reached as plastic collapse of the cell walls propagates from the loaded face into the specimen (tangential and radial) or occurs in bands in the bulk of the wood (axial) until the wood is densified, at which point stress increases sharply. Radial and tangential properties are comparable while loading axially exhibits greater stiffness, strength, and other mechanical properties. Figure adapted from [36].

### 2.2.2 Fracture

The anisotropic structure of wood also lends itself to several unique types of crack propagation designated by a pair of letters (T, R, or L). The first letter specifies the direction normal to the crack plane while the second specifies the direction of crack propagation. In some cases, a +/- sign after the two letters designates outward and inward crack propagation, respectively. The TR- system for example describes a crack plane normal to the tangential direction propagating radially inward. The nomenclature designates eight crack propagation systems as shown in Figure 8.

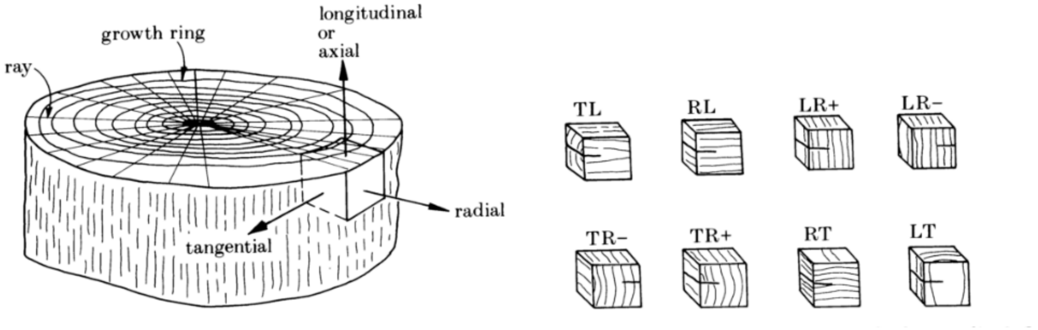

**Figure 8.** The eight systems of crack propagation in wood. The first letter designates the normal direction to the crack propagation plane while the second designates the direction of crack propagation. The +/- indicates whether the crack is growing outward or inward. Figure adapted from [6].

Wood observed under notched three-point bend tests exhibits stability up to a critical load, after which crack propagation occurs stably and then unstably usually along the grain. In low density woods the crack advances by breaking cell walls (Figure 9, A) whereas in high density woods the crack advances primarily by peeling cell walls apart at the ML layer (Figure 9, B). Vessel elements can arrest cracks (Figure 9, C) or divert crack paths via peeling (Figure 9, D) and cause discontinuous crack propagation, while ray cells can provide continuous paths of peeling [16].

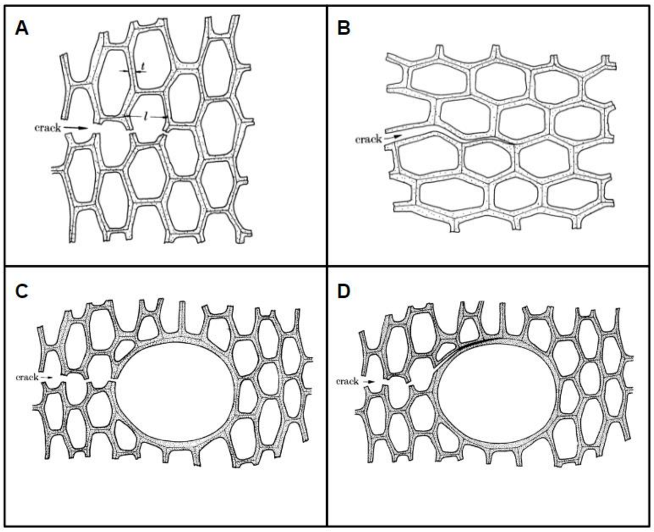

**Figure 9.** Cracks in wood propagate by (A) breaking or (B) cell wall peeling in low density and high density wood, respectively. Vessel elements can arrest cracks (C, D). Figure adapted from [16].

### 2.2.3 Predicting quasi-static mechanical behavior of wood

The bulk of wood is composed of and supported by tracheids—therefore, mechanical models of wood typically ignore structures such as vessels and rays and reduce the cellular solid to idealized tracheid elements. The earliest such attempt was by Price, A.T. [37] who modeled a tracheid as a cylindrical tube. By inferring the bulk behavior of an array of cylindrical tube elements Price suggested that $E_{Tangential}$ and $E_{Axial}$ of wood were cubically and linearly dependent on density, respectively. Srinavasan [38] built on Price's work by adding tubes normal to the axial direction to represent rays, but this expansion failed to improve the model's predictive ability and tended to overestimate $E_{Axial}$. Gibson and Ashby developed the most well known models of wood behavior by approximating tracheids as elongated hexagonal prisms rather than tubes, the dimensions of which are arbitrary as they are incorporated into a value of relative density. As seen in Table 5 the anisotropy of properties in each direction is reproduced with superior mechanical properties in axial loading in general. The radial and tangential stiffness, for example, are cubically dependent on relative density whereas axial stiffness is linearly dependent. The equations are derived analytically but require some empirical calibration via constants and can predict mechanical behavior within an order of magnitude. Additionally, they do not capture some of the more complex behaviors of plateauing and densifying seen in Figure 7. As with all biological materials a degree of heterogeneity is expected [6]:

**Table 5.** Analytically derived equations for wood properties in terms of relative density ($\rho^*/\rho_s$) [6]. $\rho^*$ = density of the wood and $\rho_s$ = density of the cell wall (~1500 kg/m$^3$).

| **Property** | **Tangential loading** | **Radial loading** | **Axial loading** |
|---|---|---|---|
| *Young's modulus* | $E_T/E_s = 0.54\ (\rho^*/\ \rho_s)^3$ | $E_R/E_s = 0.8\ (\rho^*/\ \rho_s)^3$ | $E_A/E_s = (\rho^*/\ \rho_s)$ |
| *Shear modulus* | $G_{R,T}/E_s = 0.074\ (\rho^*/\ \rho_s)^3$ | | $G_{AR,AT}/E_s = 0.074\ (\rho^*/\ \rho_s)$ |
| *Crushing strength* | $\sigma_T/\sigma_y = 0.14(\rho^*/\rho_s)^2$ | $\sigma_R/\sigma_y = 0.20(\rho^*/\rho_s)^2$ | $\sigma_A/\sigma_y = 0.34(\rho^*/\rho_s)$ |
| *Shear strength* | $\tau_{R,T}/\sigma_y = C_7(\rho^*/\ \rho_s)^2$ | | $\tau_{AR,AT}/\sigma_y = 0.086(\rho^*/\ \rho_s)$ |
| *Fracture toughness (MN/m$^{3/2}$)* | $K_{IC}\ {}^{a*} = 1.8(\rho^*/\ \rho_s)^{3/2}$ | | $K_{IC}\ {}^{n*} = 20(\rho^*/\ \rho_s)^{3/2}$ |

## 2.2.4 The strain rate dependent properties of wood

Long-term loading in construction has warranted careful study of the relation of wood strength to load duration, as under sustained load wood undergoes creep-rupture and loses strength. This trend of decreased strength with increased load duration was described using the Madison curve, in which 1x1 in clear Douglas fir beams were subjected to constant loads ranging from 60 – 95% of the average failure load of static bending tests (time to failure = 5 minutes). An empirical relationship was derived between strength and load duration over a data set with loading times ranging from 10 years to less than a second [39]. The hyperbolic curve expressed in the below equation in which SL is the stress level as a percent of ultimate strength in static loading and $t_f$ is time to failure (seconds).

$$SL = 1.83 + 108.4{t_f}^{-0.0464} \quad (1)$$

The horizontal asymptote represents the threshold of strength for infinite load duration and the vertical asymptote represents increased strength at zero time. Since the 1950s this equation has informed allowable construction designs in the National Design Specification for Wood Construction. This empirical equation, however, draws from only a single data set for impact loading conditions by Elmendorf [40] which indicated a ratio of 1.78 maximum impact load to static load (impact duration 0.015 seconds). Recent work with Split Hopkinson Pressure Bar (SHPB) tests on pine and maple of unspecified species by Gilbertson [41], [42] have supported the Madison curve even at load durations of tens of microseconds with failure occurring at loads 230% of that of static strength. What remained unclear, however, was the mechanism behind Gilbertson's observation that pine exhibited more consistent increases in compressive strength than the maple specimens did. Reid and Peng [43], [44] performed uniaxial dynamic crushing SHPB experiments (30-300 m/s) on 5 wood species (white oak, balsa, ekki, redwood, and yellow pine) ranging in density between 260-1200 kg/m$^3$ . Again, significant enhancement of crushing strength in dynamic conditions was demonstrated, and it was shown that increasing strain rates increased deformation localization in the wood species. The increased crushing strength and deformation localization with increased strain rate were explained by micro-inertial effects of the cell walls. With increasing strain rate, the cell walls' increasing resistance to acceleration (micro-inertia) by the impact force would enhance the dynamic crushing strength. Reid and Peng applied a shock model assuming rigid, perfectly plastic, locking behavior (r-p-p-l) to illustrate the micro-inertial enhancement. r-p-p-l assumes that a shock wave generating impact occurs and the stress in all the material ahead of the wave is instantly raised to the static crushing strength ($\sigma_{Cr}$) due to the material's rigid nature. As the shock wave passes the density is increased by compaction to a locking strain ($\varepsilon_L$) and raises the stress still higher to a dynamic initial crush stress ($\sigma^*$). The model is expressed in the equation below, where $\rho_0$ = initial density and v = impact velocity.

$$\sigma^* = \sigma_{Cr} + \frac{\rho_0 v^2}{\varepsilon_L} \qquad (2)$$

The r-p-p-l model accurately reflected the results of axial dynamic crushing, and all five species followed a similar stress enhancement curve with increasing impact velocity. In radial dynamic crushing, however, the five species diverged significantly from one another.

# 3 Hypothesis

This thesis aims to characterize the structure and dynamic mechanical properties of ten wood species, four of which are known for their use in impact resistant applications (black walnut, sugar maple, southern live oak, white ash) and six of which are not (African mahogany, pecan, red alder, white oak, yellow birch, yellow poplar). The former wood species must be able to withstand the dynamic loading associated with their various uses in sports equipment and weaponry.

The main hypotheses this work aims to explore are:

(I) The anatomy and structure of wood used in sporting goods and weapons are unique and help withstand dynamic load compared to commercial timbers not used for impact resistant applications.

(II) Impact resistant wood species are not only able to withstand dynamic load but exhibit weight efficiency.

# 4 Materials and Methods

Plainsawn planks of African mahogany (*Khaya ivorensis*), black walnut (*Juglans nigra)*, pecan (*Carya illinoinensis*), red alder (*Alnus rubra*), sugar maple (*Acer saccharum*), white ash (*Fraxinus Americana*), white oak (*Quercus alba*), yellow birch (*Betula alleghaniensis*), and yellow poplar (*Liriondendron tulipifera*) were purchased from commercial locations in San Diego, CA. These planks were kiln dried to ~12% moisture content. The southern live oak (*Quercus virginiana*) was generously supplied by the Berdoll Sawmill company of Austin, TX. This plainsawn plank was kiln dried to ~8% moisture content and sourced from a single ~180 year old tree growing in the region.

## 4.1 Custom drop-tower testing

A modified ASTM standard D7136/D7136 M-07 drop-tower apparatus (Figure 10) was used to test the impact strength of wood. The standard is typically used to examine the impact properties of polymer matrix composite laminate specimens of 125x75 mm dimensions. While wooden samples of such size could have easily been prepared, a custom drop-tower built at 1:5 scale by Lee, et al. [45] was used to easily compare with previous biological materials studies. The custom drop tower comprises a 3.2 mm diameter impactor tip, 1.2 kg crosshead (with maximum height 0.74 m for maximum velocity of 3.8 m/s), and 12.69 mm diameter free-standing specimen area. Using a table saw the plainsawn planks were cut into 20x20x6 mm prisms for impact testing in radial loading conditions. Axial and tangential loading conditions were neglected as these are highly unusual loading directions given the typical use of impact resistant woods.

The sawn specimens were kept in a desiccator to maintain ambient moisture by which internal moisture content may be controlled according to a lumber storage protocol [46]. Seventy one samples of African mahogany, 64 samples of black walnut, 35 samples of pecan, 45 samples of red alder, 79 samples of sugar maple, 37 samples of white ash, 45 samples of white oak, 40 samples of yellow birch, and 30 samples of yellow poplar were prepared. The impact energy was chosen starting from a failure energy followed by reducing the impact energy at intervals, with at least five samples tested per interval. The impact energy was calculated as:

$$IE_n = \frac{IE}{d_s t} \tag{3}$$

Where $IE_n$ is impact energy (IE) normalized by sample thickness (t) and cover plate aperture diameter ($d_s$). The impact energy (IE) is calculated as:

$$IE = mgh \tag{4}$$

These calculations are according to the ASTM standard D7136/D7136 M-07 [47]. The standard determines impact failure strength as the normalized impact energy at which 50% or more of samples fail (i.e. punctured by the tip, fractured, etc.)

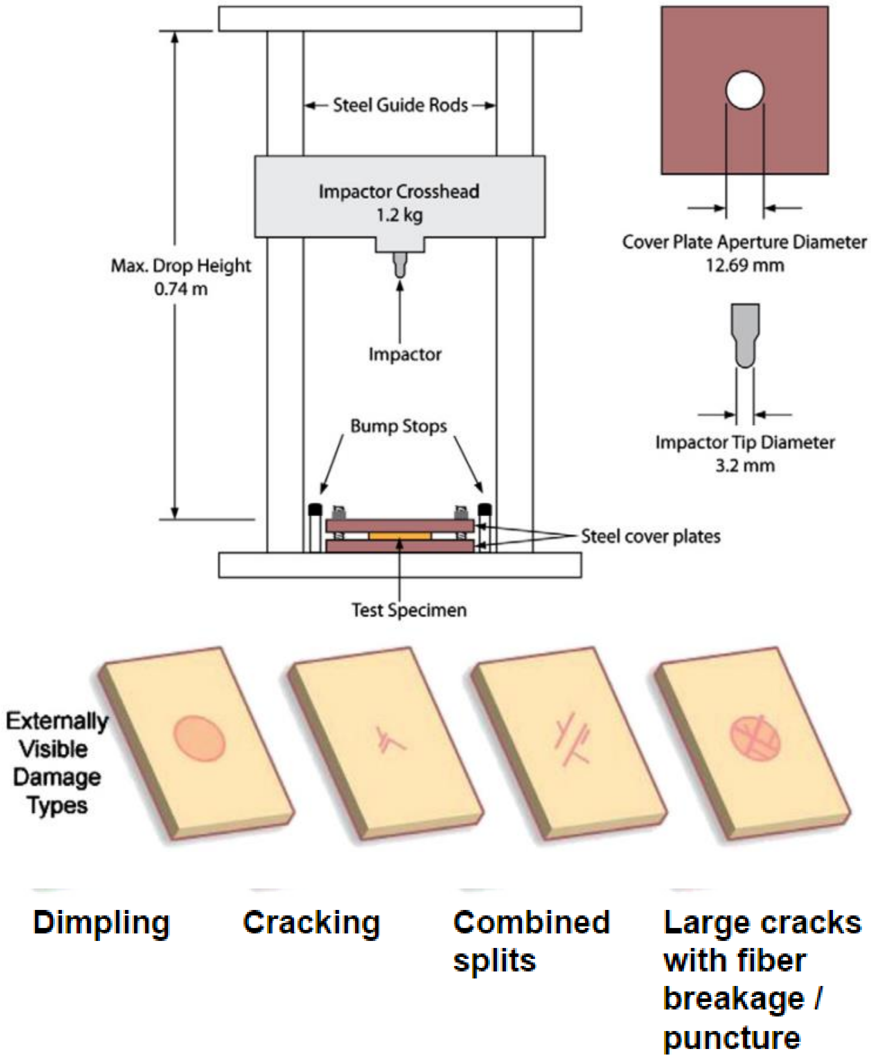

**Figure 10.** Schematic of the custom built drop tower (1:5 scale of a normal drop tower) and qualitative damage modes as defined by the ASTM standard D7136/D7136 M-07. Figure adapted from [45].

## 4.2 CEAST 9350 drop-tower testing

The custom drop-tower provides damage histograms and impact strength and allows comparisons to previously studied biological materials. It does not provide information of the material loading and strain, which can reveal mechanisms of energy absorption. Therefore an Instron CEAST model 9350 drop-tower equipped with an instrumented tip was used to obtain the time, displacement, and loading data of impacting the samples. The CEAST drop-tower was fitted with an impactor tip and cover plate of the same dimensions as the custom drop tower and samples were cut into 20x20x20 mm cubes using a table saw. Five samples of each wood species were impacted in radial loading at low velocity impacts of 1.6 m/s and impact energy of 2.9 J. The samples were thicker and the impact slower as the information desired was not the damage progression but the manner of the load-displacement curve (i.e. peak load, displacement, deceleration).

## 4.3 Quasi-static compression testing

It is well established that in quasi-static conditions wood mechanical properties are density dependent, but the aim of this study was to investigate wood behavior in dynamic conditions. To understand whether the observed phenomena are a consequence of dynamic loading or not quasi-static compressive tests in the radial loading direction were conducted on wood samples. Sample geometry (20x20x6 mm) and tip dimensions were identical as those described in section 4.1. Samples were tested to failure at displacement rate of 0.2 mm/s to allow comparison of the relative amount of energy absorbed by each wood species to failure in quasi-static and dynamic conditions.

## 4.4 Scanning electron microscopy (SEM)

Wood samples were cut to 20x20x6 mm squares using a band saw, after which they were impacted. Samples that failed and were fractured into two or more pieces were selected and were sputter coated with iridium at 85µA for 10 seconds to reduce charging using an Emitech K575X

Sputter Coater. Samples were then imaged using a Zeiss Sigma 500 Field Emission Scanning Electron Microscope.

# 5 Results and Discussion

## 5.1 Custom drop-tower and quasi-static compression testing

Cut samples were measured and weighed to obtain density values:

**Table 6.** Average density of impacted wood samples. n = number of samples tested.

| **Wood species** | **Density (kg/m$^3$)** | **n** |
|---|---|---|
| *Southern live oak* | 1100 ± 100 | 37 |
| *Pecan* | 820 ± 35 | 35 |
| *White oak* | 740 ± 38 | 47 |
| *Sugar maple* | 710 ± 53 | 79 |
| *African mahogany* | 670 ± 57 | 71 |
| *Black walnut* | 650 ± 32 | 68 |
| *White ash* | 600 ± 26 | 42 |
| *Yellow birch* | 600 ± 15 | 40 |
| *Yellow poplar* | 560 ± 19 | 30 |
| *Red alder* | 450 ± 16 | 45 |

The damage mode of the impacted wood was visually assessed according to the modified ASTM standard D7136/D7136 M-07. In addition to the damage modes of dimpling, cracking, delamination, and failure described in the ASTM a failure mode of splitting along the wood grain was commonly observed. Most woods split as their main failure mode, with no damage visible on the face opposite of the impacted surface, and rupturing was observed only in pecan, red alder, and white ash. Ruptured wood did not shatter and the sections remained cohesive even after failing. In Figure 11 are the representative damage progressions of splitting and rupturing.

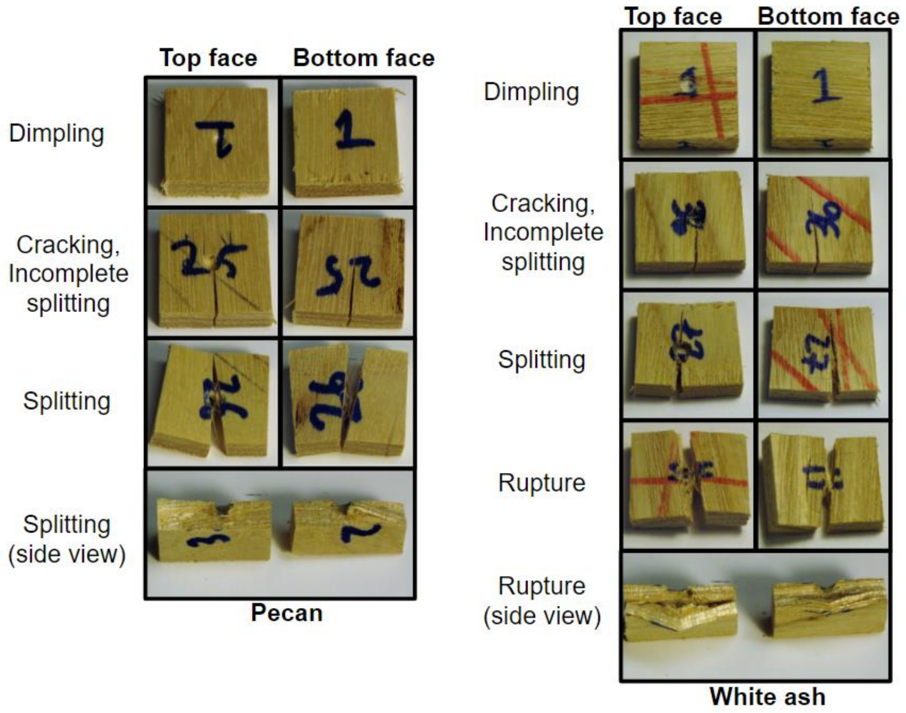

**Figure 11.** The damage progression of pecan (left) and white ash (right). Most wood species failed in the manner depicted on the left in which a clean split is formed along the grain of the wood. Red alder and white ash, however, exhibited a unique failure mode of rupture in which internal delamination and damage on the opposite face of the impacted surface were visible.

As seen in Table 6, red alder represented the most lightweight wood species tested (450 ± 16 kg/m$^3$). Its failure mechanism seemed to confirm the quasi-static observation that crack propagation in low density wood occurs via cell wall breaking rather than peeling. Pecan (820 ± 35 kg/m$^3$) and white ash (600 ± 26 kg/m$^3$), however, were of above average density and exhibited rupturing behavior while other woods of comparable density split and failed via cell wall peeling. This may be caused by low density zones in the vessel bands of ring porous woods. The observed failure mode of white ash also confirms anecdotes that white ash baseball bats are safer than maple baseball bats in that they do not fragment into dangerous flying pieces and remain stuck together on breaking [48], [49]. The development of damage progression for each wood species is shown in Figure 12.

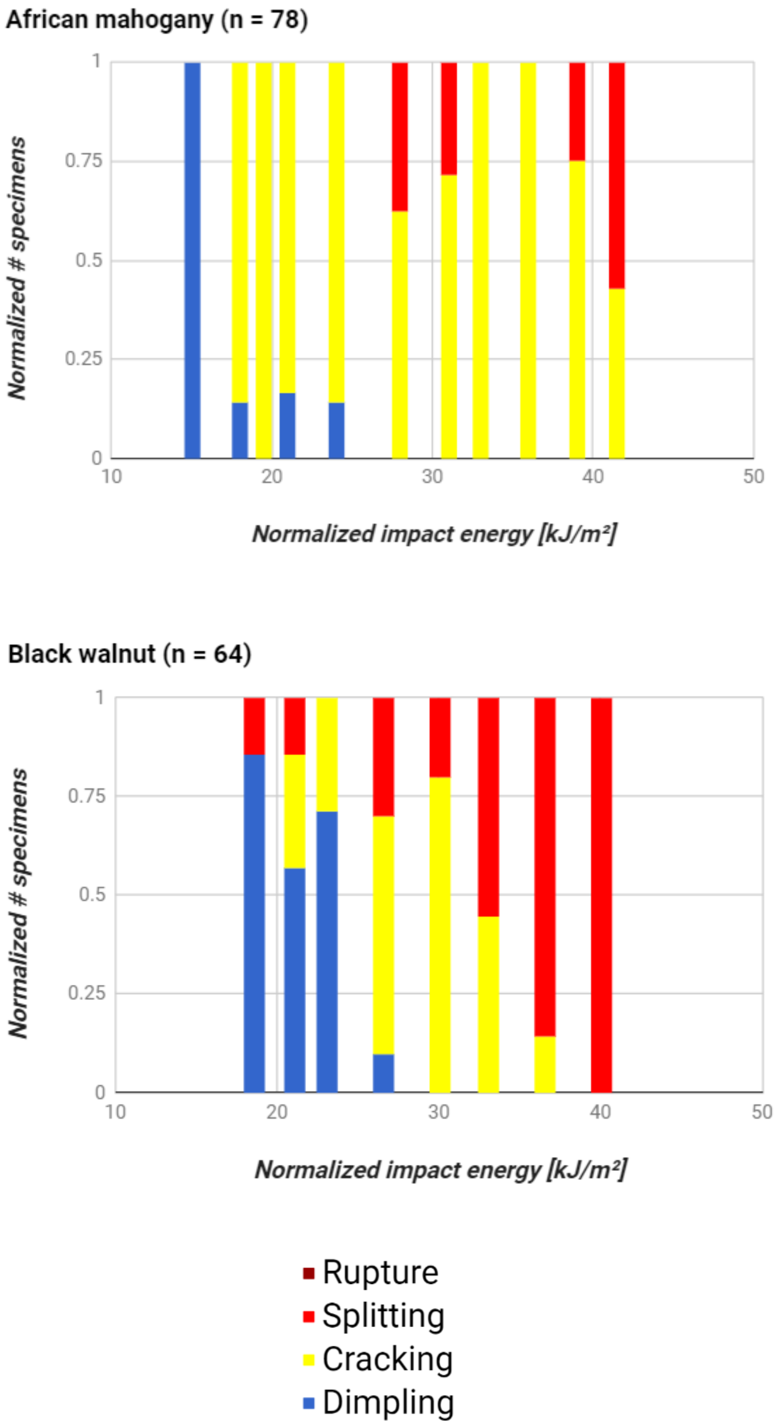

**Figure 12.** Impact damage histograms for wood (in alphabetical order).

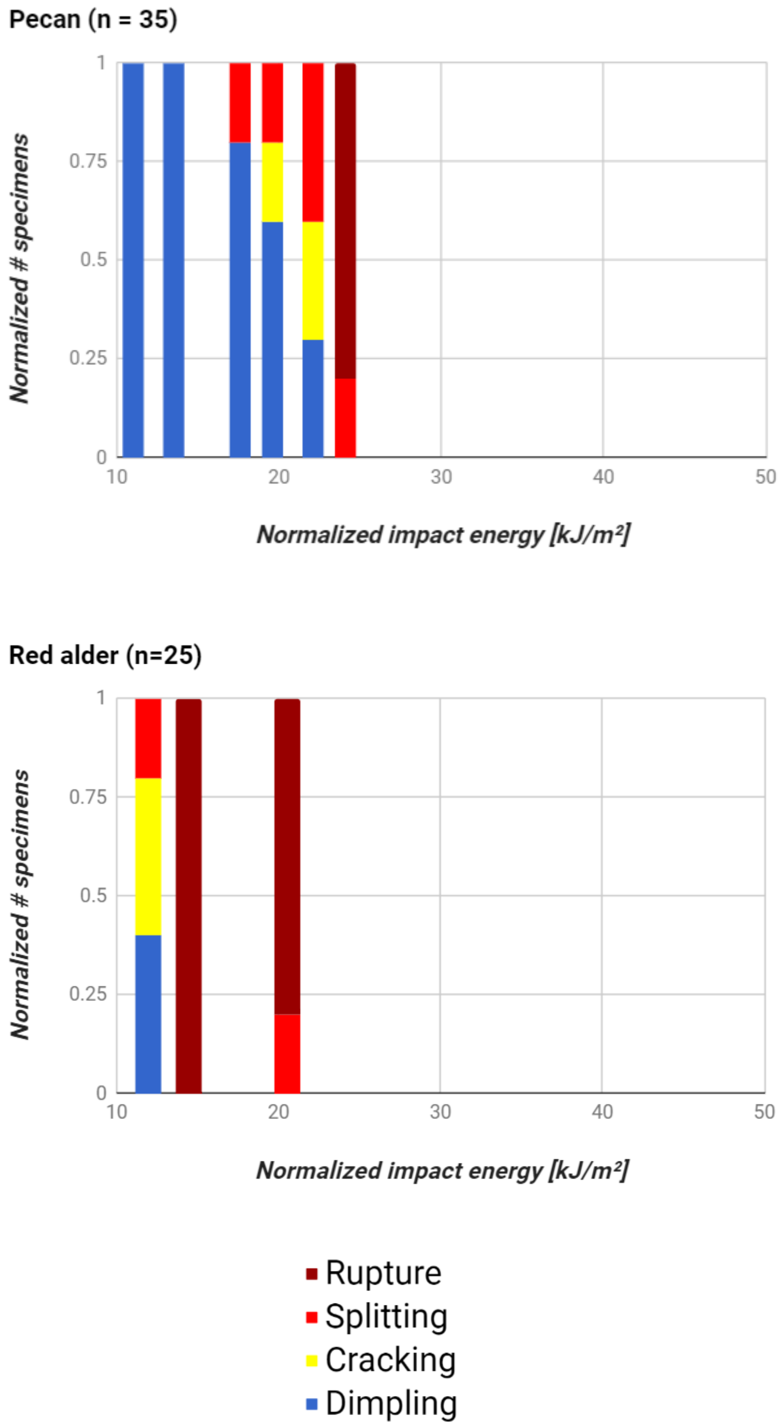

**Figure 12 (cont.).** Impact damage histograms for wood (in alphabetical order).

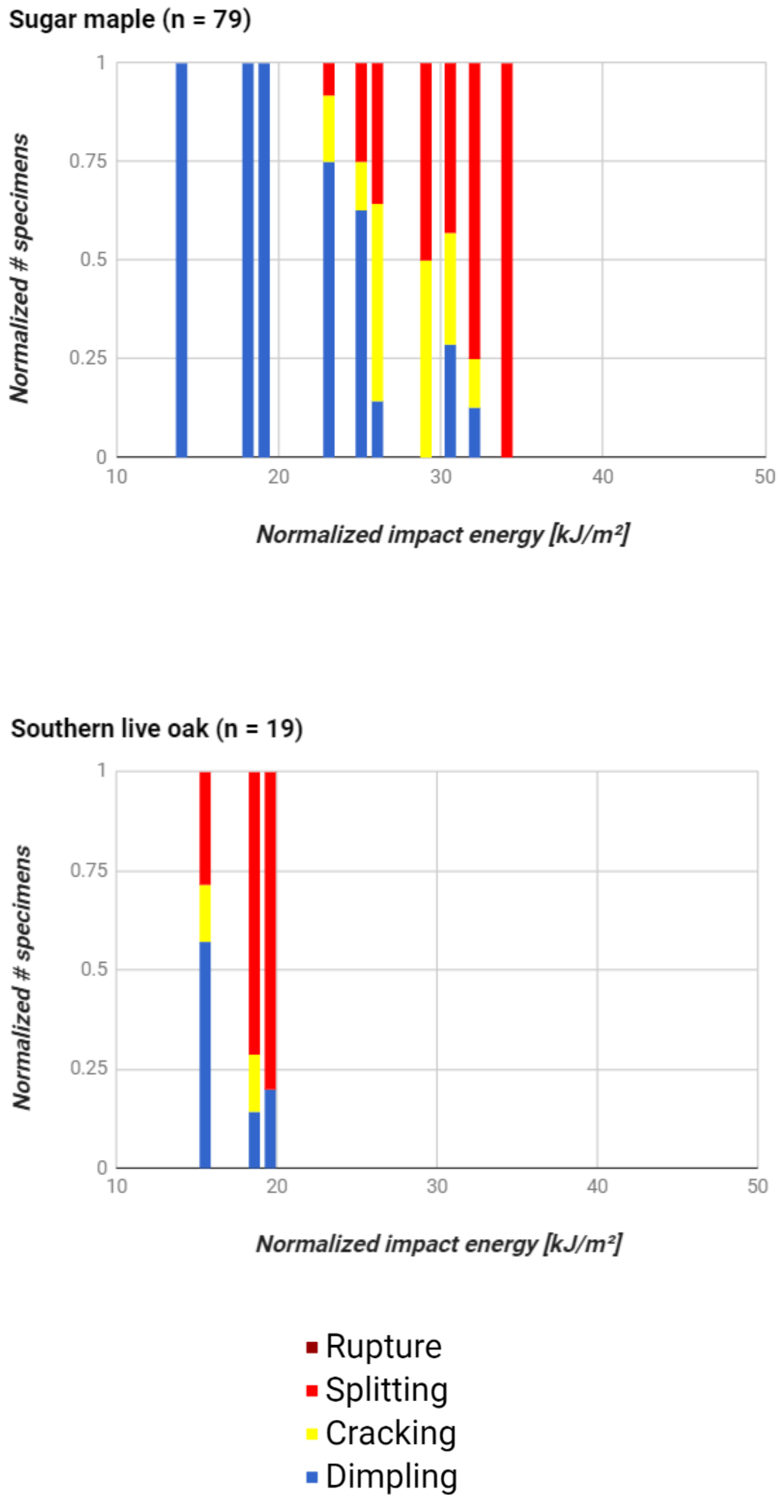

**Figure 12 (cont.).** Impact damage histograms for wood (in alphabetical order).

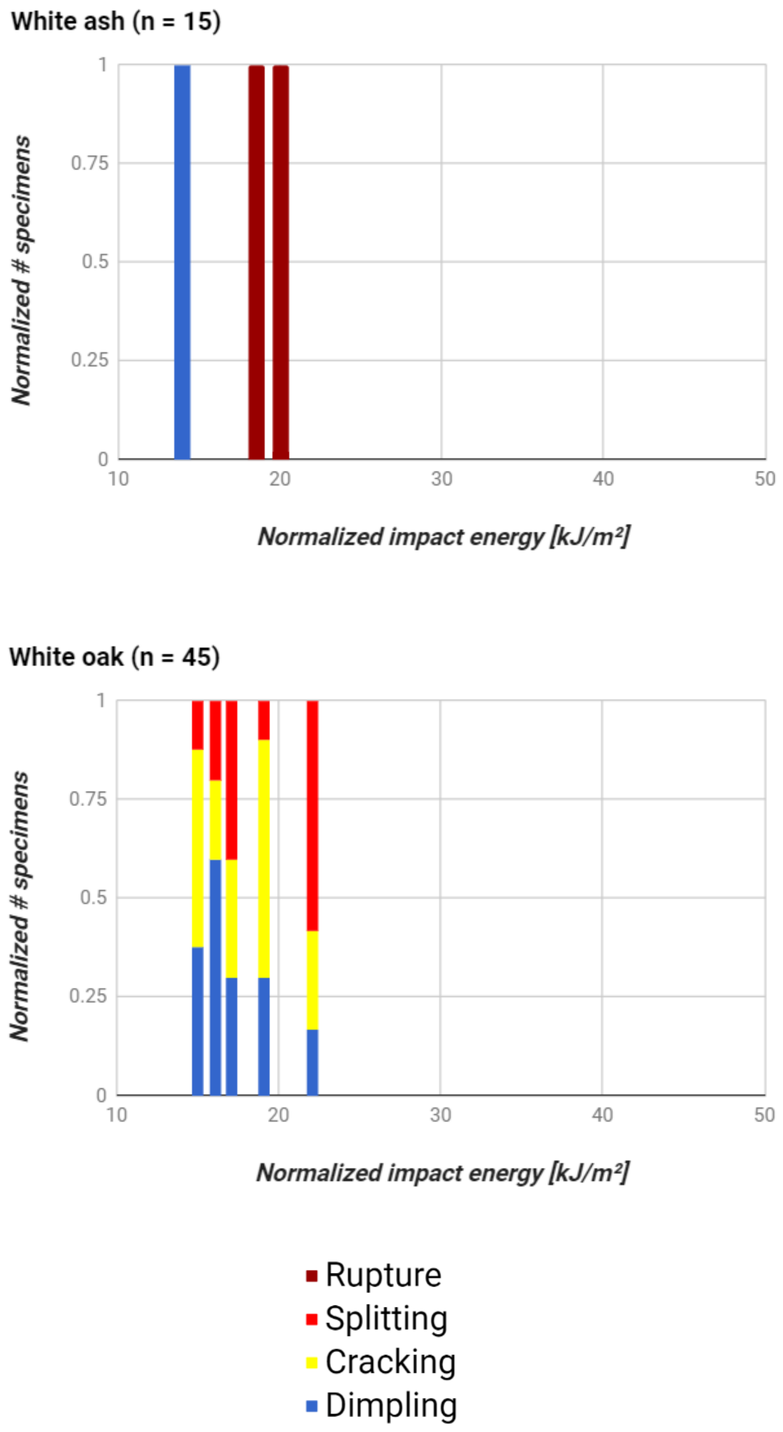

**Figure 12 (cont.).** Impact damage histograms for wood (in alphabetical order).

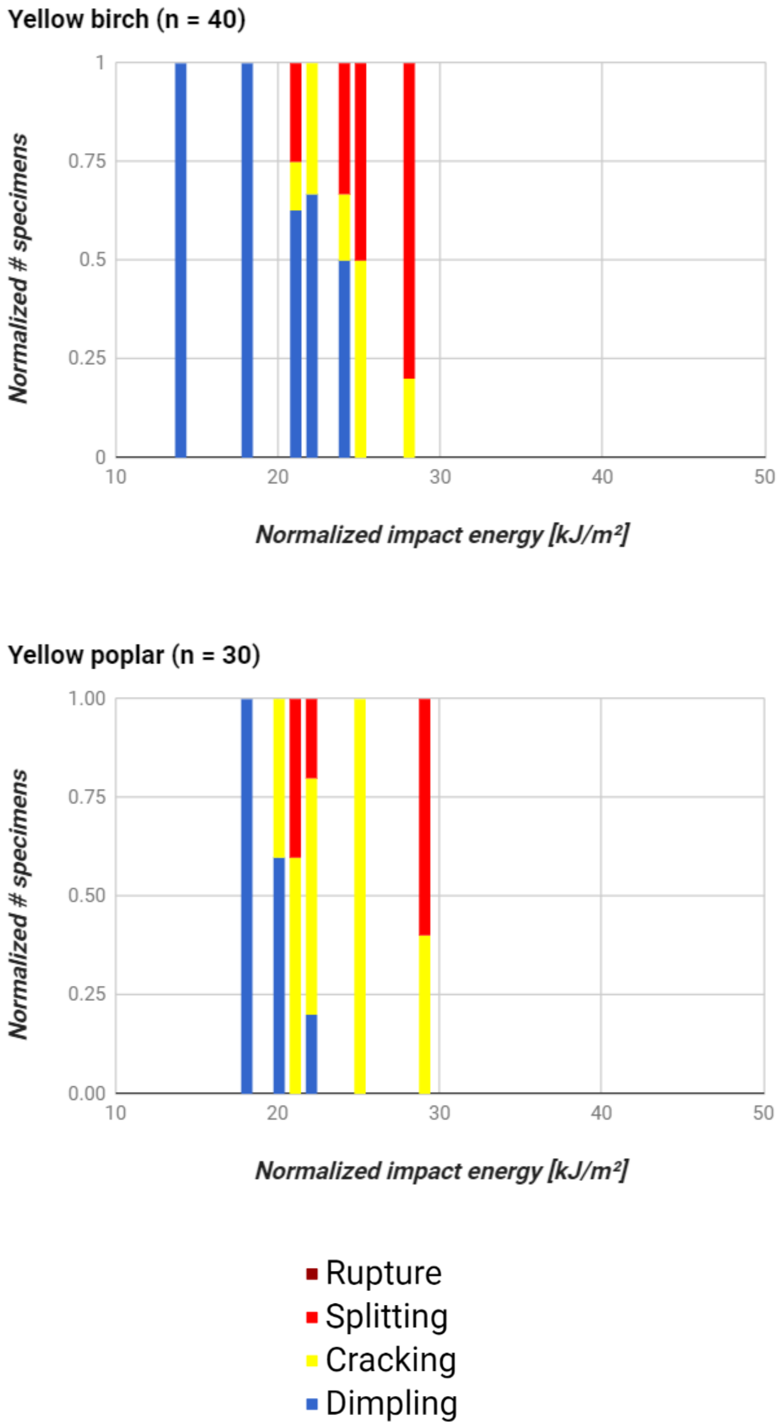

**Figure 12.** Impact damage histograms for wood (in alphabetical order).

**Table 7.** Average normalized energy of impact failure of wood samples. n = total number of samples tested.

| **Wood species** | **Normalized energy of failure (kJ/m$^2$)** | **n** |
|---|---|---|
| African mahogany | 42 | 78 |
| Black walnut | 33 | 64 |
| Sugar maple | 29 | 79 |
| Yellow poplar | 29 | 30 |
| Yellow birch | 25 | 40 |
| Pecan | 24 | 35 |
| White oak | 22 | 45 |
| White ash | 18 | 15 |
| Southern live oak | 18 | 19 |
| Red alder | 14 | 25 |

All wood specimens exhibited dimples of increasing diameter and depth with increasing impact energy. African mahogany progressed immediately from dimpling to cracking at impact energies as low as 16 kJ/m$^2$, but did not reach failure (>50% of five or more samples at a given energy) until 42 kJ/m$^2$. Of the tested tree species African mahogany was the only one to exhibit this damage progression behavior of early cracking onset and late failure. Furthermore, cracks and splits that occurred in African mahogany tended to change direction as viewed from the side while cracks tended to propagate straight through most other wood specimens and produce neatly cleaved pieces (Figure 14). African mahogany's ability to change crack propagation direction may be related to the orientation of its tracheids and vessels in the axial system, or "grain." In some species tracheid growth occurs at a slight angle for several years only to reverse direction later, alternating several times throughout the tree's life. Because tree growth occurs at the radial periphery this produces layers of alternating grain growth direction called "interlocking grain" (Figure 13, TOP) which produce the swirling patterns that make interlocking grain woods aesthetically desirable (Figure 13, A and B). In most tree species, however, growth occurs in the vertical direction with little change in direction or resulting in "straight grain" (Figure 13, C).

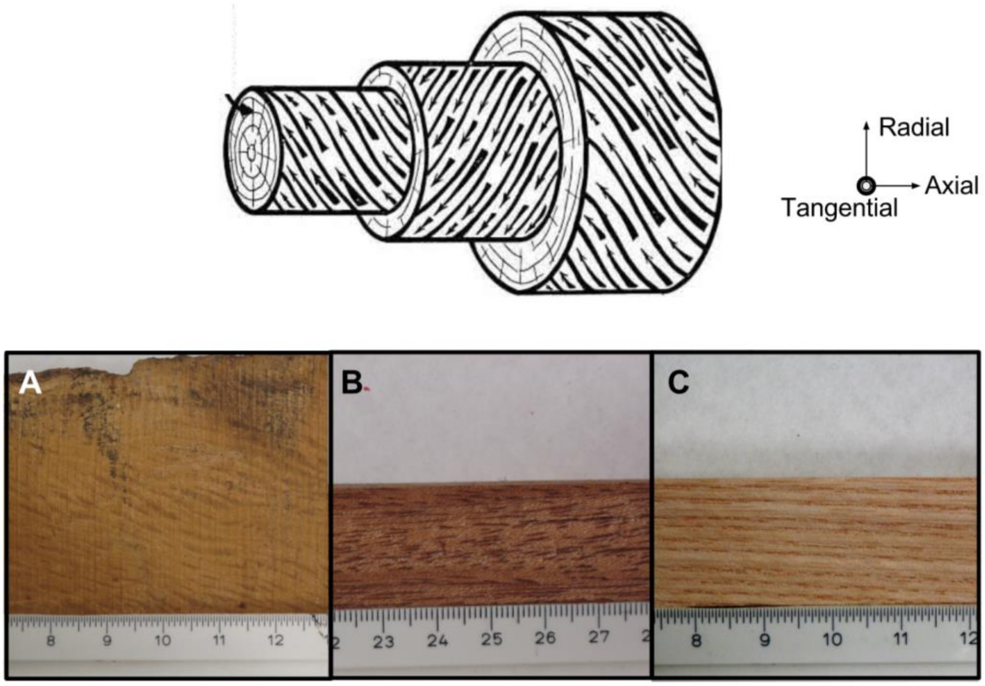

**Figure 13.** Interlocking grain [43] (TOP) as seen in (A) southern live oak and (B) African mahogany compared to straight grain in (C) alder. Figure adapted from cited source.

Southern live oak, another species with interlocking grain, exhibited similar behavior in failure: fractured pieces produced wavy and irregular surfaces in contrast to the flat and smooth surfaces observed in other wood species. Unlike African mahogany, however, the southern live oak failed at the low impact energy of 19 kJ/$m^2$ and the dimples left behind were very shallow. The highly brittle mechanical response of southern live oak is surprising, considering its historic use in warships and Aztec weapons [50], [51].

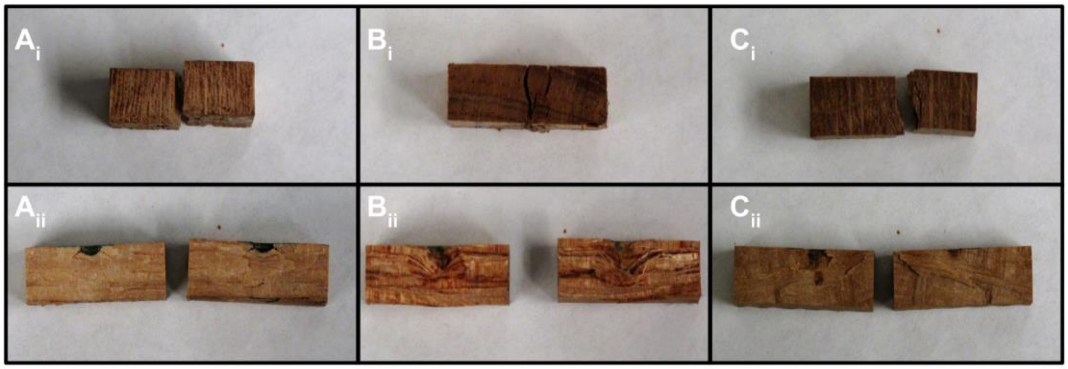

**Figure 14.** Splitting in (A) white oak, (B) African mahogany, (C) and southern live oak. While splitting in white oak produces cleanly cleaved and flat surfaces (as in all other tree species found to split rather than rupture), splitting in African mahogany and southern live oak produces wavy cracks.

However, the differing moisture content (~8% compared to ~12% for other species) may have contributed to its brittle and hard behavior as drying wood packs its fibers together. Furthermore, southern live oak has not been heavily used for over a century due to difficulties cutting and drying the wood as well as its long growth cycle—it is possible that the knowledge of how to effectively prepare this species for impact resistant applications was lost.

A common wood structure also seemed to result in similar behavior in red alder, sugar maple, yellow birch, and yellow poplar. These species all exhibit a uniform distribution of vessel elements in the end-grain, called a diffuse porous arrangement, and exhibited a very similar damage progression of dimpling at low energies followed by consistently increasing frequencies of cracking and splitting behavior with greater impact energies. No rupturing behavior was observed in these species. Sugar maple failed at energy of 32 kJ/m$^2$ and even exhibited dimpling in a small fraction of samples at 31 and 32 kJ/m$^2$. Yellow birch and yellow poplar samples failed at slightly lower energies of 28 and 29 kJ/m$^2$, respectively, but also exhibited greater penetration depths. Red alder is also diffuse porous but ruptured rather than split at 14.5 kJ/m$^2$—as previously discussed this is likely caused by its very low density relative to the other diffuse porous tree species, making cell wall breaking energetically favorable to cell wall peeling.

The black walnut exhibited high impact resistance with a failure energy of 29 kJ/m$^2$ but tended to occasionally split or crack at lower impact energies. Though comparable in density and failure behavior to sugar maple (Table 6), its structure is semi-diffuse porous (vessel elements are present throughout the end grain, but decrease in diameter from the beginning of one growth ring to the end of the next). This is the only species of semi-diffuse porous tree examined and the effect of this vessel distribution is unclear, however.

Pecan and white ash, like red alder, exhibited rupturing failure despite being significantly denser ($\rho_{\text{Pecan}} = 820 \pm 35$ kg/m$^3$, $\rho_{\text{white ash}} = 600 \pm 26$ kg/m$^3$, $\rho_{\text{red alder}} = 450 \pm 16$ kg/m$^3$). These tree species are ring porous, meaning that their vessels are confined to narrow bands that correspond to the spring and summer seasons of growth between growth rings. No vessels occur in the growth regions corresponding to the fall and winter. Though bands of sap channels tend to arrest crack propagation in quasi-static conditions, it seems that they have the opposite effect in dynamic loading resulting in dramatic rupturing and low energy failure. Pecan failed at an energy of 22 kJ/m$^2$ and exhibited both splitting and rupturing failure modes, while white ash failed at 18.5 kJ/m$^2$. White oak shares this ring porous structure and failed at similarly low impact energies of 22 kJ/m$^2$, but did not exhibit rupturing: most specimens failed by splitting cleanly.

The impact energy of each failed sample can be plotted against its density to better understand the efficiency of each wood species relative to one another, as shown in Figure 15.

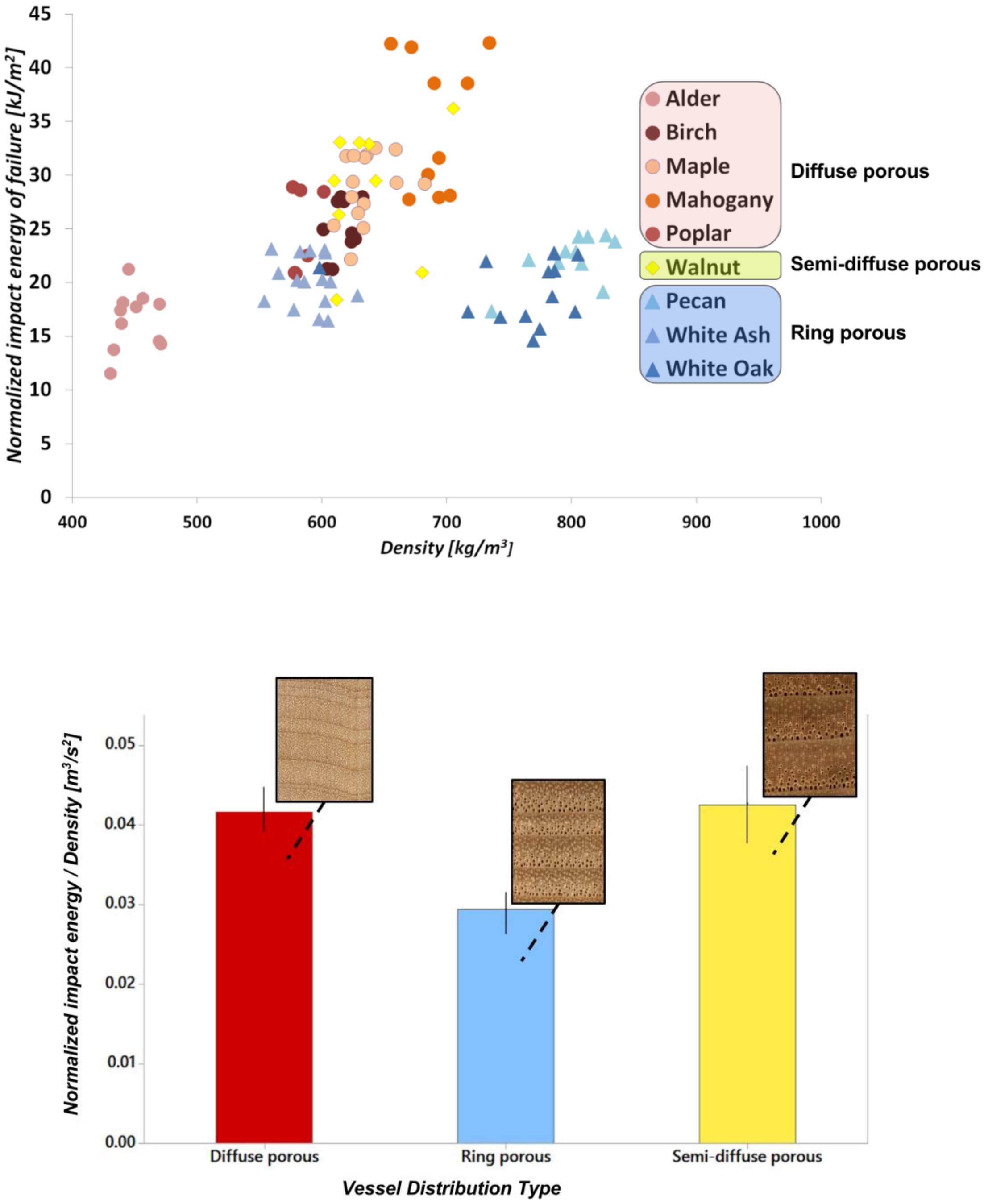

**Figure 15.** (TOP) The normalized impact energy of failure plotted against the sample density provides insight into the efficiency of each wood species. While the impact resistance of wood with diffuse porous and semi-diffuse porous vessel distributions is significantly improved by density, that of ring porous woods is not. (BOTTOM) Averaging the ratio of normalized impact energy of failure to density reveals a ~33% difference between the ability of diffuse and semi-diffuse porous woods to absorb impact compared to ring porous woods.

Separating the wood species by vessel distribution type points to a correlation with impact resistance: while increasing density improved the impact resistance of diffuse porous trees, ring porous trees consistently failed at approximately ~20 kJ/m$^2$ across ~550-850 kg/m$^3$ range (discussed in Figures 18-20). Red alder, a diffuse porous tree of average density 450 kg/m$^3$, exhibited similar strength to, a ring porous tree of average density 820 kg/m$^3$. The difference in structure between the diffuse porous, ring porous, and semi-diffuse porous trees is clear in the optical micrographs (Figure 16).

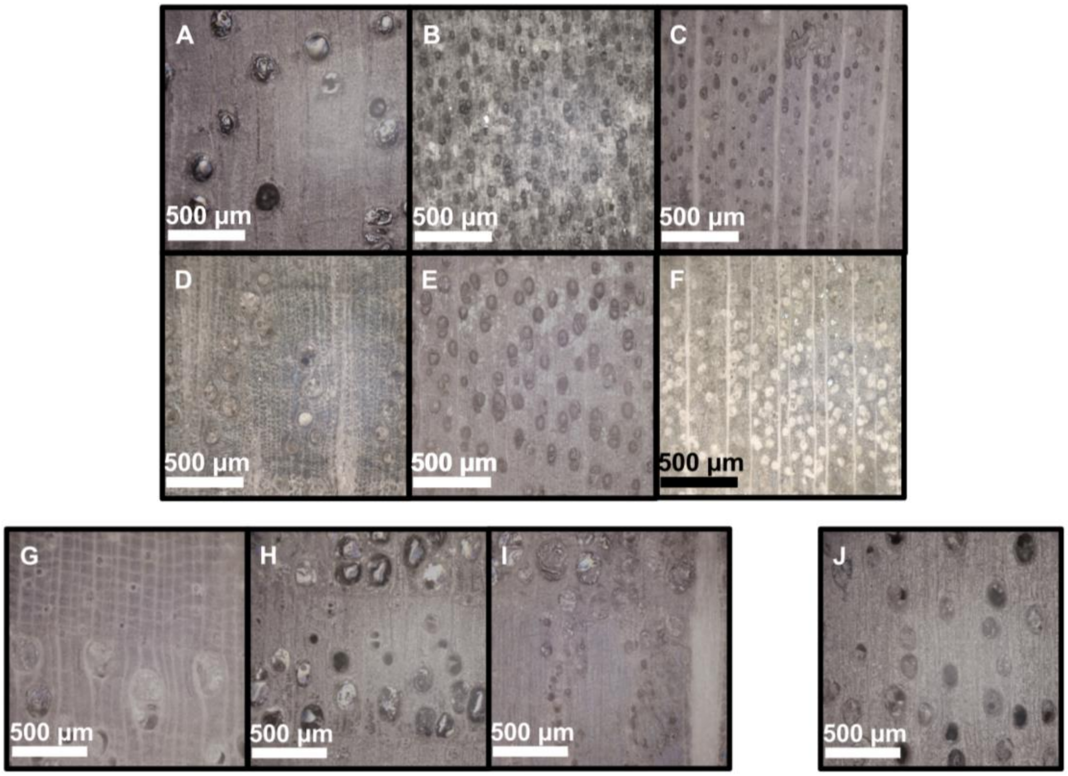

**Figure 16.** Optical micrographs of polished end grain images of wood. (TOP) Diffuse porous species are (A) African mahogany, (B) red alder, (C) sugar maple, (D) southern live oak, (E) yellow birch, and (F) yellow poplar. (BOTTOM LEFT) Ring porous species are (G) pecan, (H) white ash, and (I) white oak. (BOTTOM RIGHT) (J) Black walnut is semi-diffuse porous.

It is possible, however, that the selected ring porous species happened to be hard and therefore unable to absorb as much shock as equally dense but soft species, for example. The hardness of wood is typically measured by Janka hardness, or the load required to embed an 11.28 mm ball to half its diameter (Table 8).

**Table 8.** Literature values for Janka hardness of wood species at 12% moisture content [52], [53]

| **Wood species** | **Janka hardness (N)** |
|---|---|
| *Yellow poplar* | 2400 |
| *Red alder* | 2600 |
| *African mahogany* | 3800 |
| *Black walnut* | 4500 |
| *Yellow birch* | 5600 |
| *White ash* | 5900 |
| *White oak* | 6000 |
| *Sugar maple* | 6400 |
| *Pecan* | 8100 |

Analysis of variance (ANOVA) was used to understand whether these multiple factors of vessel distribution, density, and Janka hardness had a statistically significant effect on the wood impact resistance. A general linear model was applied to analyze the response (normalized impact energy of failure) of samples treating vessel distribution as a categorical factor and Janka hardness and density as covariates. Southern live oak was not included in the analysis due to its different heat treatment and moisture content, both of which influence mechanical properties [46].

**Table 9.** Results of wood impact resistance examined using analysis of variance (ANOVA) with a general linear model. *S* = standard error, *P* = probability value of null hypothesis, *F* = Fisher test value, $R^2$ = coefficient of determination

| **Variable** | **S [kJ/m$^2$]** | **P (0-1)** | **F** | **R$^2$** |
|---|---|---|---|---|
| *Density* | 5.68 | 0.008 | 7.61 | 4.85% |
| *Vessel distribution type* | 5.27 | 0.003 | 6.74 | 19.4% |
| *Janka hardness* | 5.82 | 0.8 | 0.08 | 0.170% |
| *Density & vessel distribution type* | 3.79 | < 0.0005 | 11.24 | 61.0% |
| *Density & Janka hardness* | 4.87 | N/A | 3.45 | 32.9% |
| *Vessel distribution type & Janka hardness* | 5.01 | N/A | 6.82 | 28.7% |

The standard error (S) refers to the statistical accuracy of the model, or its standard deviation of response distribution, and its units are those of the response (kJ/m$^2$). The probability value of null hypothesis (P) indicates the likelihood that the observed relationship occurred purely by chance. A low P-value indicates that the null hypothesis is false (i.e. not random) or that the null hypothesis is true but a highly unlikely series of results occurred. The Fisher test value (F) is the ratio of variance between groups and variance within groups and quantifies statistical significance alongside the P-value. If the null hypothesis is true, then the F-test value should be close to one and the P-value high. Finally, the coefficient of determination ($R^2$.) describes the percentage of variability explained by the model, or how close the response data are to the fitted regression line.

Each factor on its own provides a poor predictive model of wood dynamic behavior. Janka hardness has close to no relationship with wood impact resistance with a P-value of 0.8 and $R^2$ of 0.170%--even when combined with density or vessel distribution in a multi-variable model Janka hardness offers no insight (P-values are not calculated here due to replicates of Janka hardness, because of using literature values). Density appears somewhat related to dynamic mechanical properties as seen in its moderately low P-value (0.008) and moderately high F-test value (7.61), but clearly fails to provide a complete picture ($R^2$ = 4.85%). The same could be said of vessel distribution as a factor, with P-value, F-test value, and $R^2$ of 0.003, 6.74, 19.4%, respectively.

Combining vessel distribution and density yields a statistically significant result that stands far above other models with a P-value, F-test value, and $R^2$ of <0.0005, 11.24, and 61.0%. The accuracy is also significantly improved to a standard error of +/-3.79 kJ/$m^2$ (though some heterogeneity in results is expected, as in all biological material mechanical properties).

To understand whether this interaction between vessel distribution and density is unique to impact loading conditions, the experiment was replicated in quasi-static conditions (0.2 mm/s) with identical geometry.

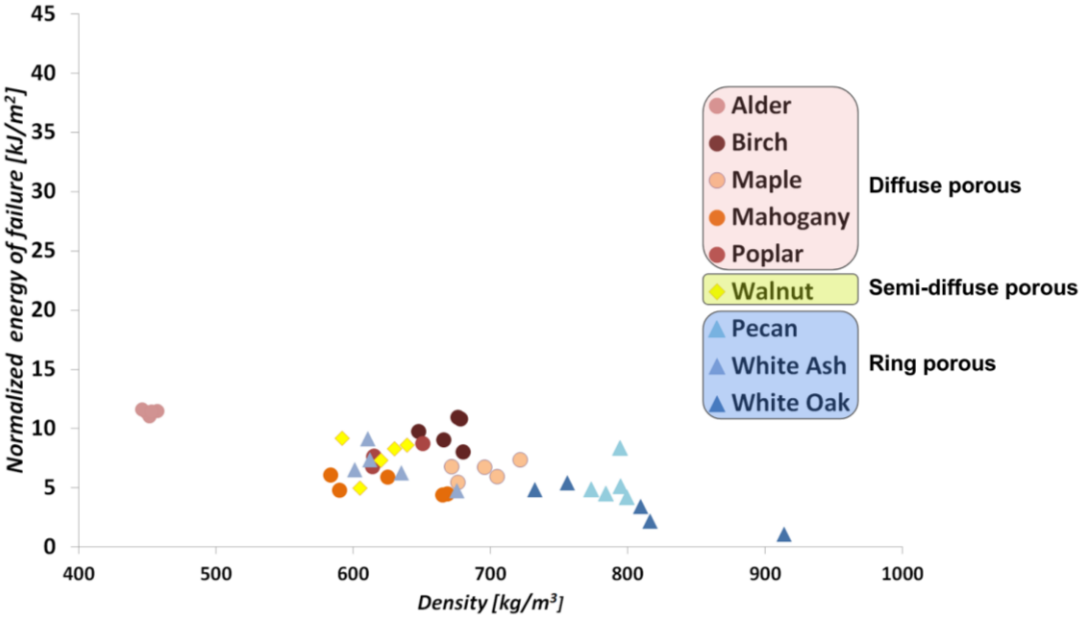

**Figure 17.** Work to failure normalized by sample geometry in quasi-static (0.2 mm/s) compressive loading conditions in the radial direction. The loading geometry is identical to that in the custom drop-tower test.

Compared to the results of Figure 15, it is immediately clear that density is a far more powerful predictor of work to failure in quasi-static conditions than in dynamic loading, albeit with some heterogeneity. ANOVA was repeated for these results (Table 10).

**Table 10.** Results of wood quasi-static work to fracture examined using analysis of variance (ANOVA) with a general linear model. *S* = standard error, *P* = probability value of null hypothesis, *F* = Fisher test value, $R^2$ = coefficient of determination

| **Variable** | **S [kJ/m$^2$]** | **P (0-1)** | **F** | **R$^2$** |
|---|---|---|---|---|
| *Density* | 1.77 | <0.0005 | 50.7 | 54.1% |
| *Vessel distribution* | 2.27 | 0.002 | 7.49 | 26.3% |
| *Janka hardness* | 1.28 | <0.0005 | 17.9 | 79.9% |
| *Density & vessel distribution* | 1.82 | 0.79 | 0.23 | 55.3% |
| *Density & Janka hardness* | 1.18 | N/A | 1.00 | 87.1% |
| *Vessel distribution & Janka hardness* | 2.26 | N/A | 18.5 | 28.3% |

Statistical analysis confirms the observation from Figure 17 that the predictive ability of density is far improved in quasi-static conditions than in dynamic: standard error, probability value of null hypothesis, Fisher test value, and coefficient of determination are far better compared to values in Table 9. The vessel distribution as an independent factor maintains a statistical significance similar to those in impact, but exhibits a diminished interaction with density. The F-test value of 0.23 indicates that the variance in work to fracture between groups is lower than that within each group, but combined with a P value close to 1 (0.79) it is more likely these are random results. The Janka hardness is unsurprisingly related to the work to fracture, as it is the load required to embed an 11.28 mm ball to half its diameter (a similar geometry to our experiment). Although density and Janka hardness are independently important factors, the F-test value of 1 when the two factors were combined indicates there is no meaningful interaction.

To understand the observation that ring porous trees are as efficient as diffuse porous trees in quasi-static loading and not in impact loading, SEM images of quasi-statically compressed (0.2 mm/s) and impacted (1.6 m/s) white ash were examined. Tubule structures found in other biological materials such hooves, teeth, and fish scales improve fracture toughness and energy absorption through a variety of ways: they can act as crack arrestors by removing stress singularities at a crack tip (Figure 9), collapse when compressed, or scatter stress pulses generated by impact [1]. Quasi-statically compressed samples (Figure 18) revealed vessel collapse propagating from the loading face like tubules in ram horns. Impacted samples (Figure 19) on the other hand revealed crack propagation into the tangential bands of vessels (RT mode) through cell wall peeling and breaking. A simplified diagram (Figure 20) contrasts the two damage modes. These SEM images explain not only why the rupturing damage mode was observed in ring porous tree species (Figure 12), but also why increased density provided no improvement in impact resistance (Figure 15). The ability of cracks to propagate into these concentrated low density vessel regions is inherent to the ring porous structure. In both samples, largely intact vessels were observed and their role is unclear without *in situ* observational capabilities or simulation.

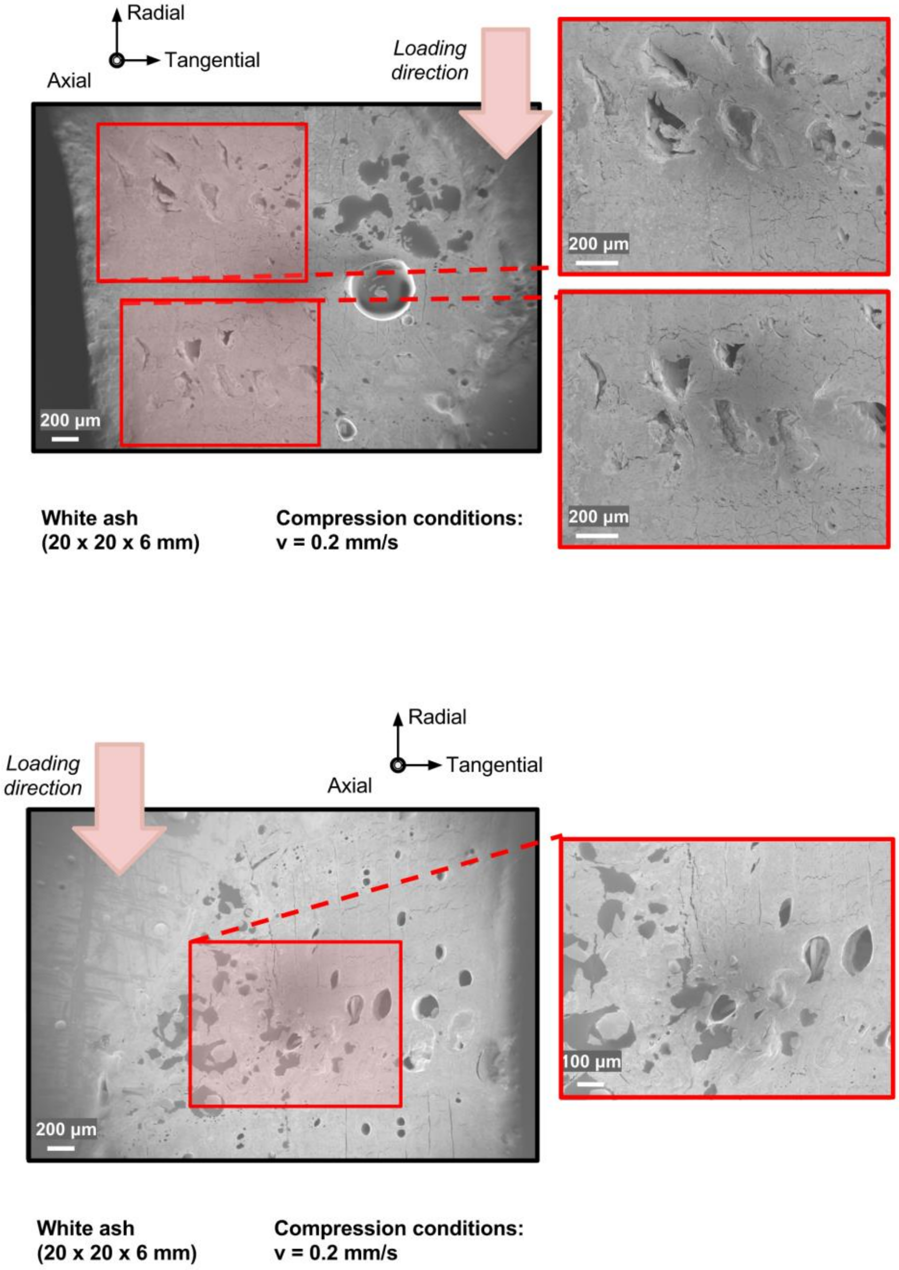

**Figure 18.** Axial cross sections of quasi-statically compressed white ash (ring porous). Vessel compression propagating from the loading face is the predominant mechanisms of damage absorption.

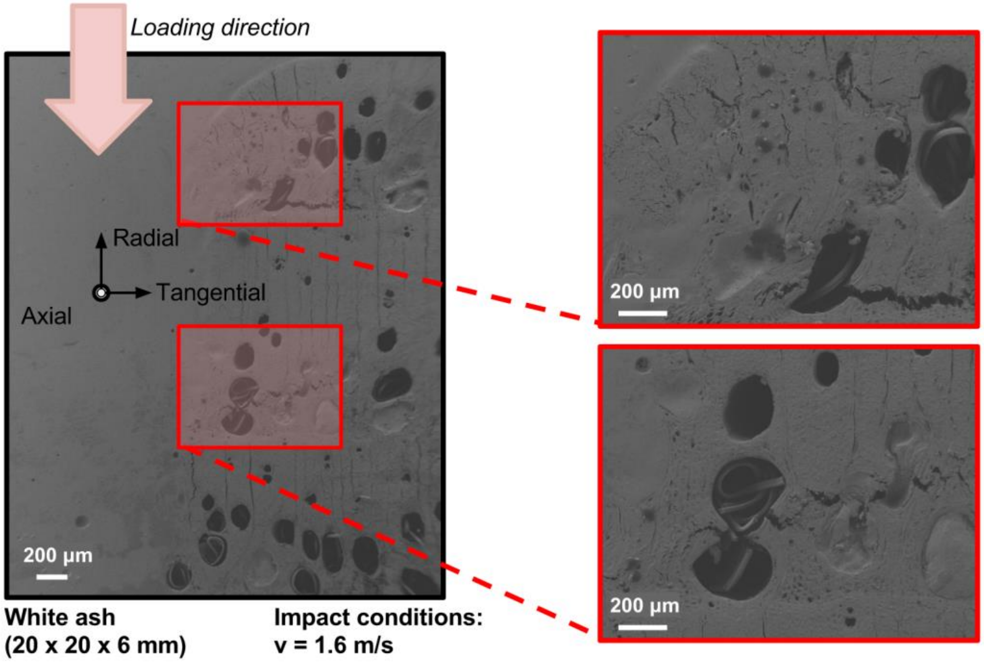

**Figure 19.** Axial cross sections of impacted white ash (ring porous). Crack propagation into the tangential bands of vessels through cell wall peeling and breaking was visible, explaining the rupturing damage mode observed in ring porous tree species regardless of density.

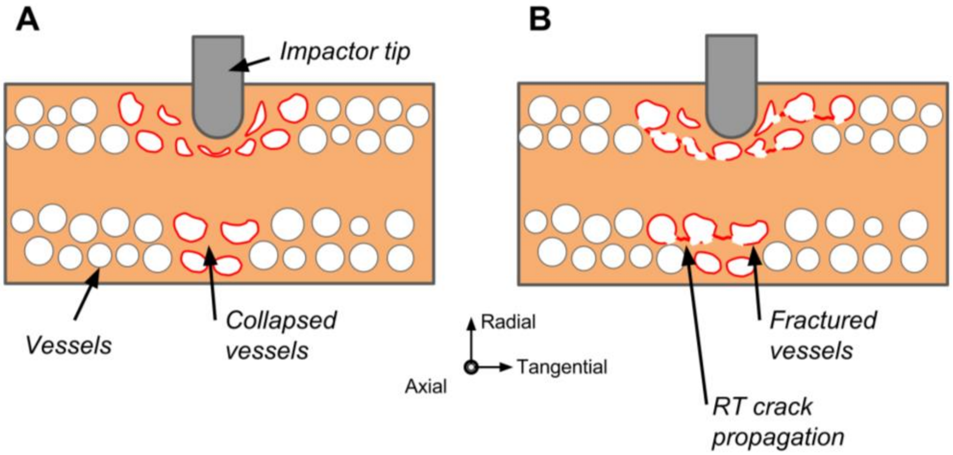

**Figure 20.** Diagram representing vessel deformation in (A) quasi-static and (B) impact conditions in ring porous wood. Whereas vessels collapsed and absorbed the energy of quasi-static deformation, vessels bands in impact became low density crack paths.

The loading conditions on the vessels are complex but in simplifying them to the classic problem of a stress concentration around a hole, two mechanisms for RT crack propagation emerge. The first is that shearing by the tip on the tangential face ($\tau_{\text{Tangential, Axial}}$) can generate tensile forces with a threefold stress concentration factor (Figure 21). The second is that compression in the tangential direction by the penetrating tip generated a radial tensile strain causing crack propagation (Figure 22).

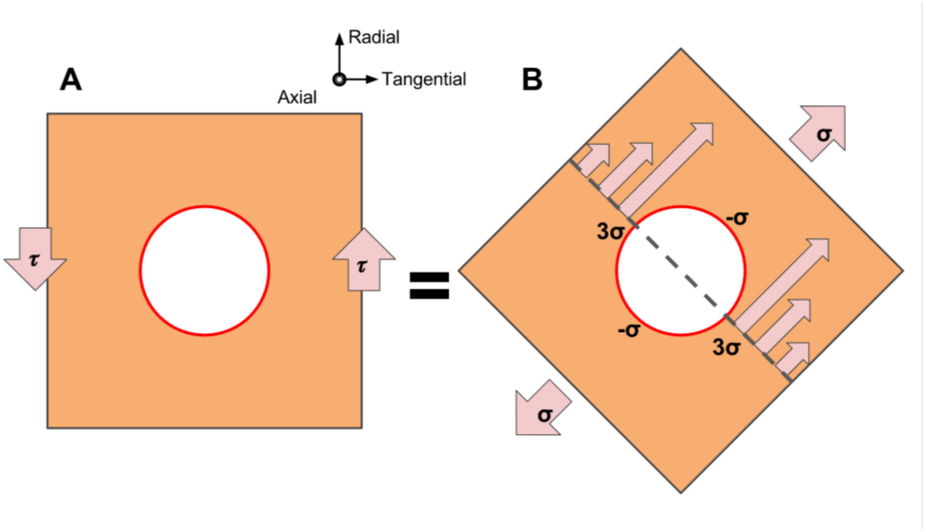

**Figure 21.** Penetration of the impact tip generated (A) shearing force ($\tau_{\text{Tangential, Axial}}$) that could be decomposed into tensile elements (B), resulting in the classic problem of a stress concentration around a hole and crack propagation in the RT direction.

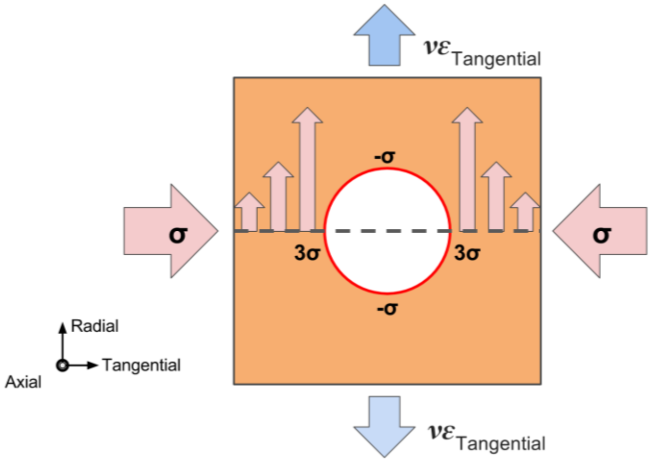

**Figure 22.** Penetration of the impact tip generated a compressive force in the tangential direction and complimentary axial strain, exerting tension that could be expressed as a stress concentration around a hole.

The loading conditions are once again complex, however, and finite element analysis could shed further light on these mechanisms in the future.

## 5.2 CEAST 9350 drop-tower testing

The CEAST 9350 drop-tower was deployed to understand the time, displacement, and loading data of the various wood species in impact—again, the samples were thicker (20x20x20 mm) and the impact slower (1.6 m/s) as the information desired was not the damage progression but the peak load, displacement, deceleration. Failure would generate large noise.

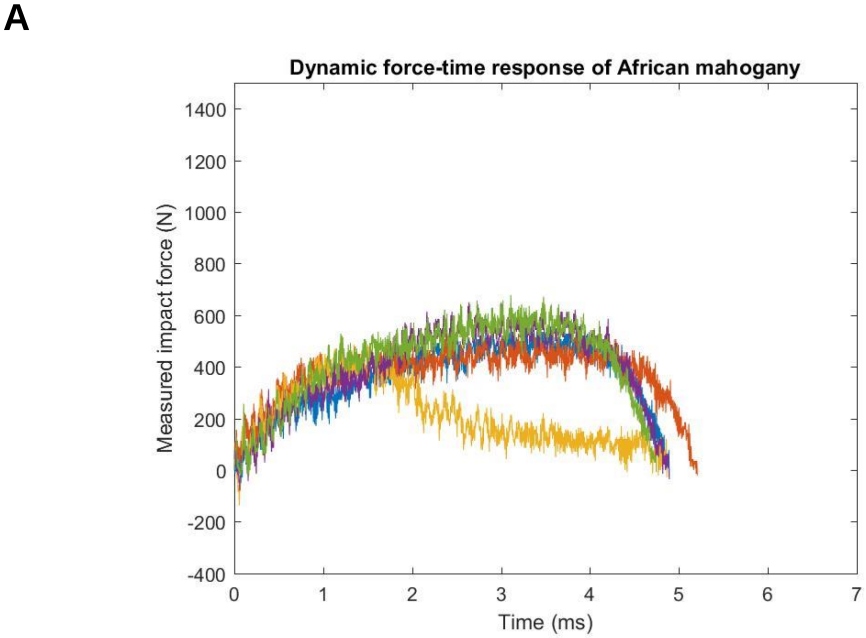

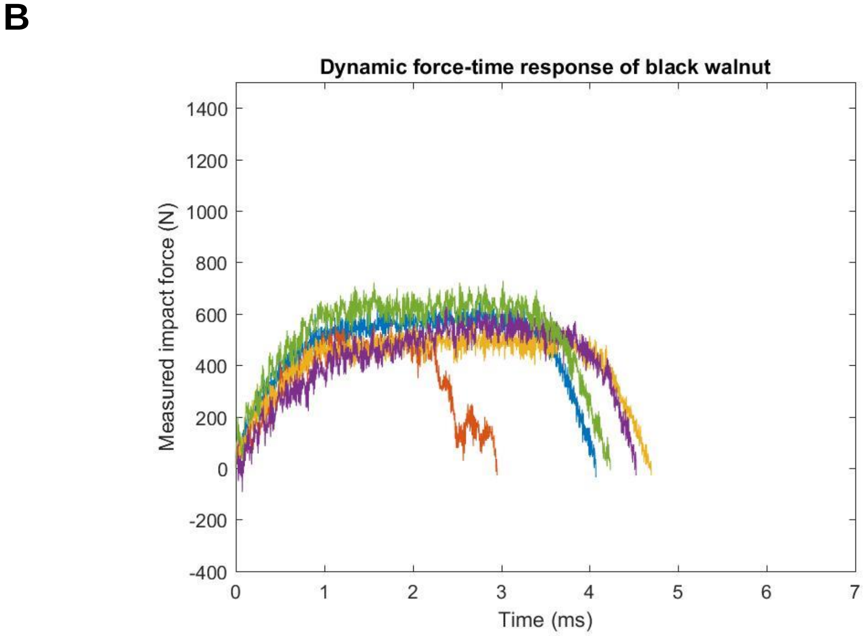

**Figure 23.** Force-time response of tree species impacted in the CEAST 9350 (in alphabetical order). Samples of dimensions 20x20x20 mm, impact velocity 1.6 m/s, and impact energy of 2.9 J. The ASTM D7136 does not recommend smoothing of the data as the oscillations represent reverberations which are a component of the material response to impact. (A) African mahogany exhibited low amplitude oscillations and peak forces similar to (B) black walnut, indicating a strong ability to absorb shock.

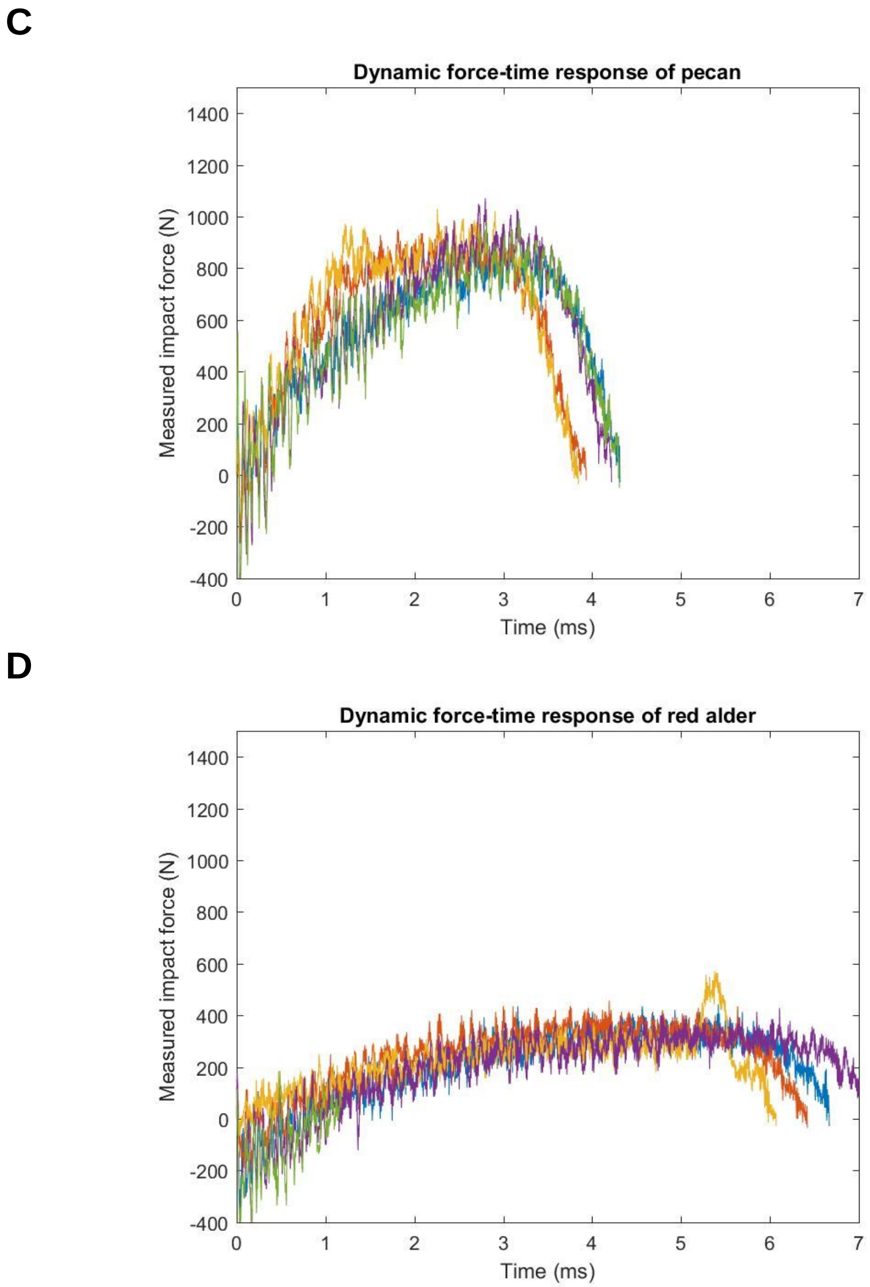

**Figure 23. (cont.)** Force-time response of tree species impacted in the CEAST 9350 (in alphabetical order). Samples of dimensions 20x20x20 mm, impact velocity 1.6 m/s, and impact energy of 2.9 J. (C) Pecan exhibited high amplitude oscillations at the initial impact moment and large peak forces of approximately ~800 N, whereas (D) red alder maintained low peak forces indicating a gradual deceleration of the impactor tip.

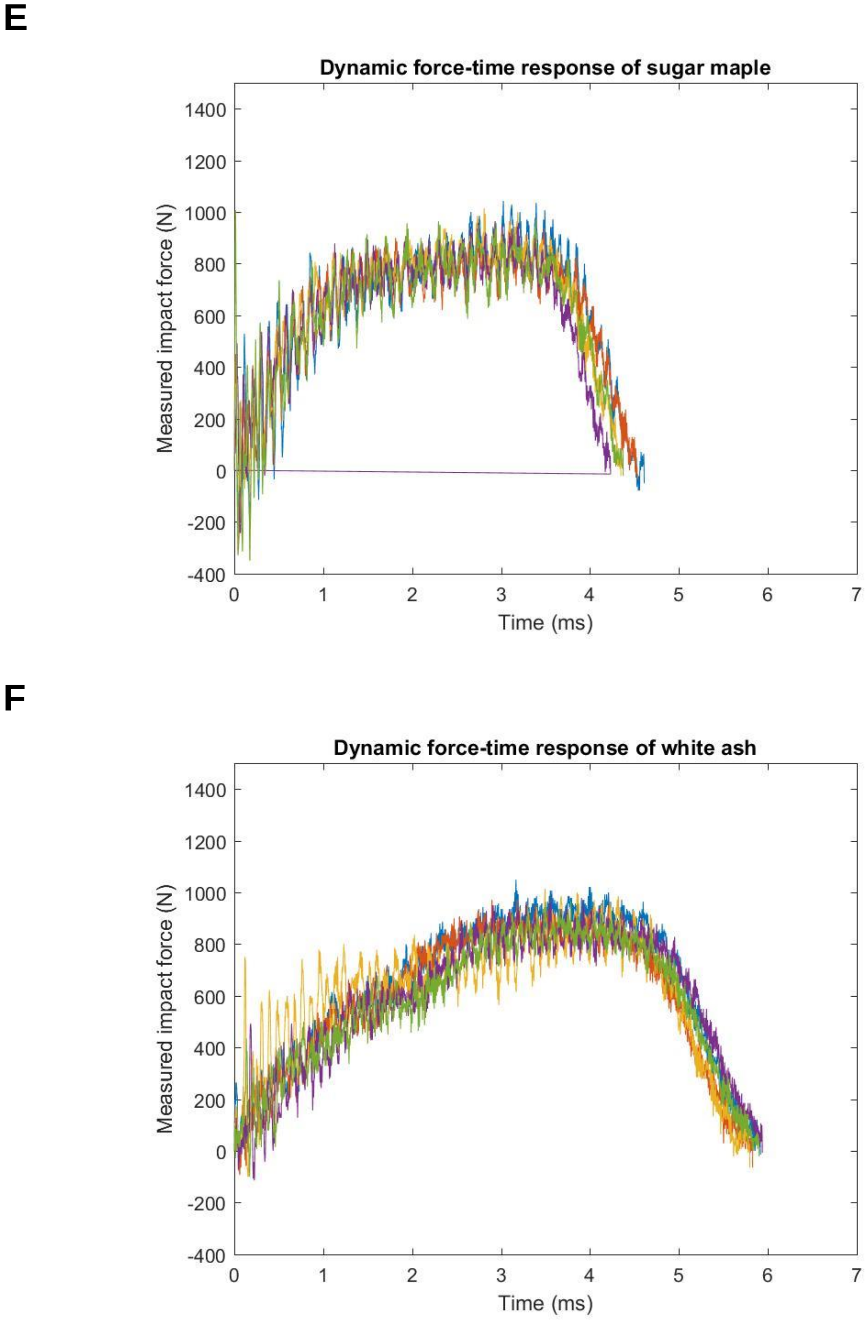

**Figure 23. (cont.)** Force-time response of tree species impacted in the CEAST 9350 (in alphabetical order). Samples of dimensions 20x20x20 mm, impact velocity 1.6 m/s, and impact energy of 2.9 J. (E) Sugar maple's normalized impact energy of failure was comparable to that of walnut (Table 7) but force-time measurements revealed greater peak forces and oscillations, pointing to lower shock absorbance. (F) White ash samples exhibited high oscillations at the initial moment of impact and peak load of approximately ~800N, like pecan (Figure 23, C).

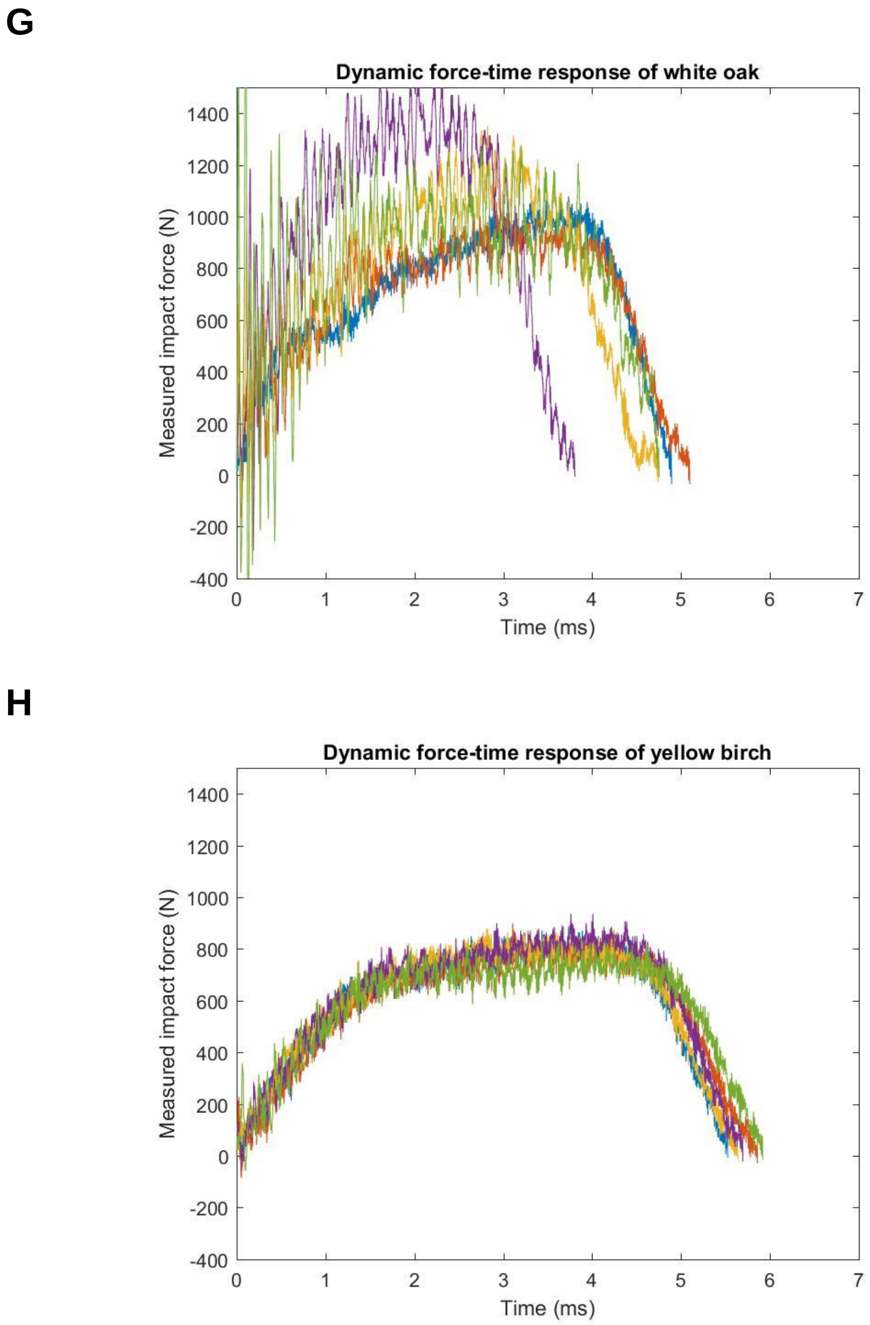

**Figure 23. (cont.)** Force-time response of tree species impacted in the CEAST 9350 (in alphabetical order). Samples of dimensions 20x20x20 mm, impact velocity 1.6 m/s, and impact energy of 2.9 J. (G) White oak exhibited high oscillations at the initial moment of impact and high peak forces. (H) Yellow birch exhibited low peak forces and oscillations indicating strong shock absorption.

**I**

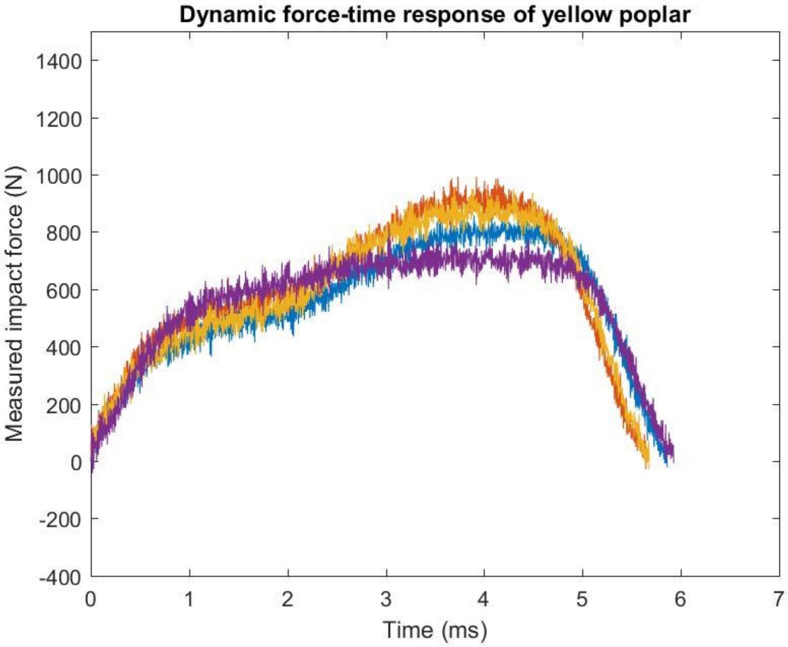

**Figure 23. (cont.)** Force-time response of tree species impacted in the CEAST 9350 (in alphabetical order). Samples of dimensions 20x20x20 mm, impact velocity 1.6 m/s, and impact energy of 2.9 J. Samples exhibited a particularly gradual ramp up to peak load compared to other species indicating progressive damage absorption.

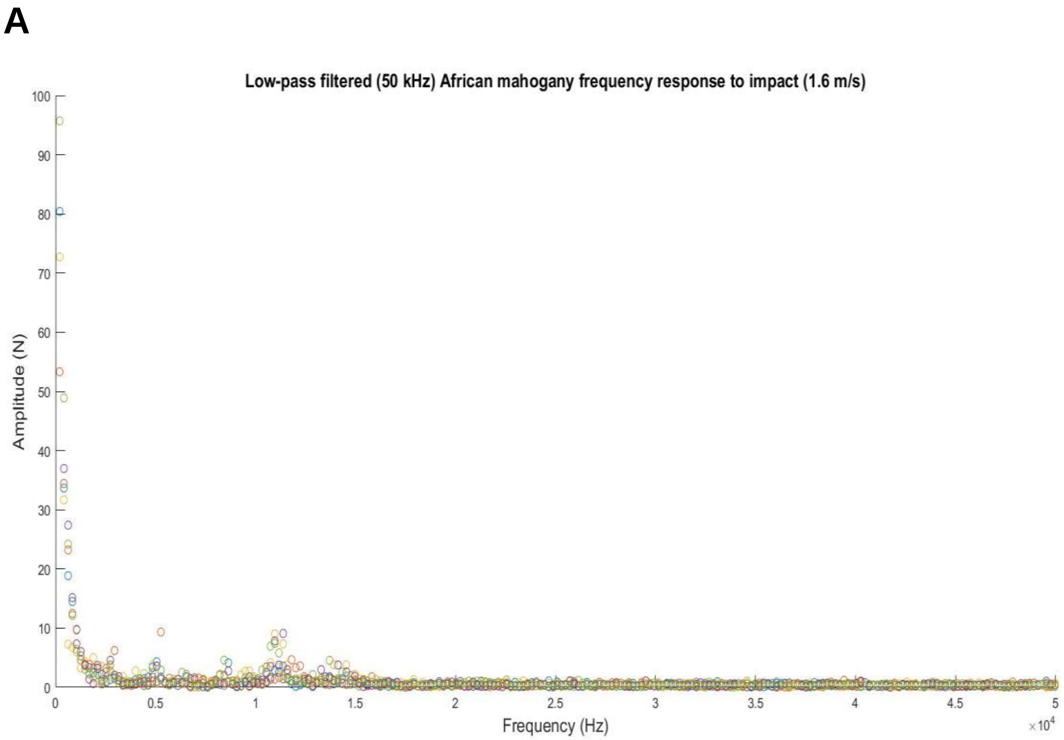

**Figure 24.** Low-pass filtered frequency response of tree species impacted in the CEAST 9350 (in alphabetical order). Samples of dimensions 20x20x20 mm, impact velocity 1.6 m/s, and impact energy of 2.9 J. Samples exhibited tight grouping at 5, 11 kHz of ~10 N amplitude, consistent with the low amplitude oscillations noted in Figure 23, A.

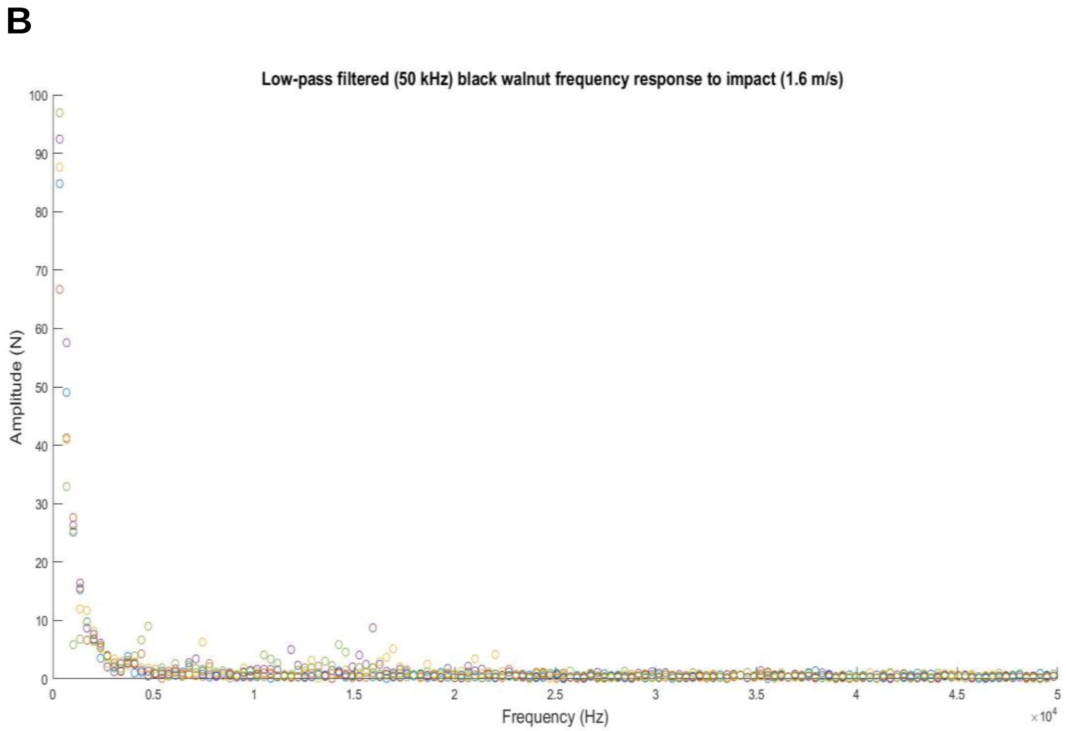

**Figure 24. (cont.)** Low-pass filtered frequency response of tree species impacted in the CEAST 9350 (in alphabetical order). Samples of dimensions 20x20x20 mm, impact velocity 1.6 m/s, and impact energy of 2.9 J. Samples exhibited grouping at ~ 5, 15 kHz of ~10 N amplitude, consistent with the low amplitude oscillations noted in Figure 23, B.

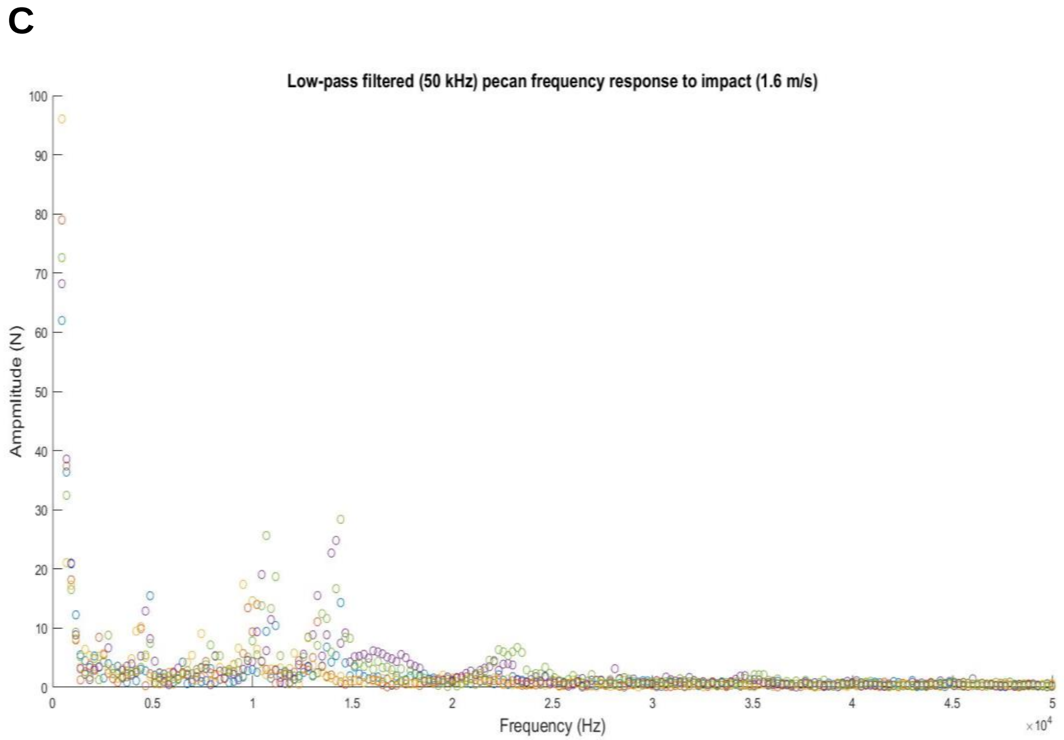

**Figure 24. (cont.)** Low-pass filtered frequency response of tree species impacted in the CEAST 9350 (in alphabetical order). Samples of dimensions 20x20x20 mm, impact velocity 1.6 m/s, and impact energy of 2.9 J. Samples exhibited tight grouping at ~5, 10, and 15 kHz of large ~ 20 N amplitude, consistent with the high amplitude oscillations noted in Figure 23, C.

**D**

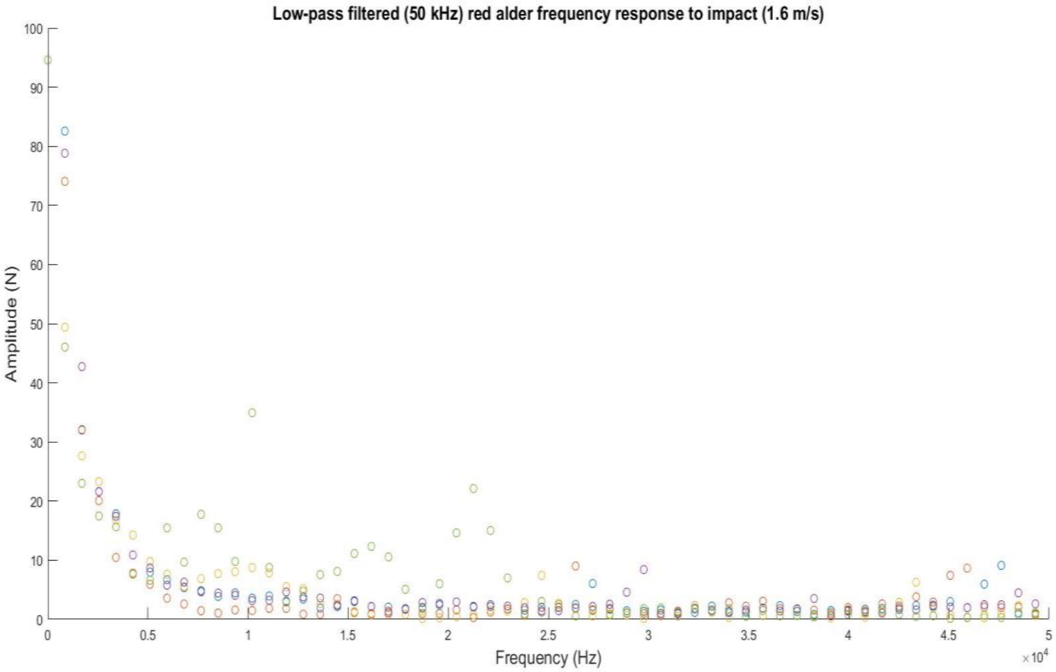

**Figure 24. (cont.)** Low-pass filtered frequency response of tree species impacted in the CEAST 9350 (in alphabetical order). Samples of dimensions 20x20x20 mm, impact velocity 1.6 m/s, and impact energy of 2.9 J. Samples exhibited a broad response across various frequencies.

**E**

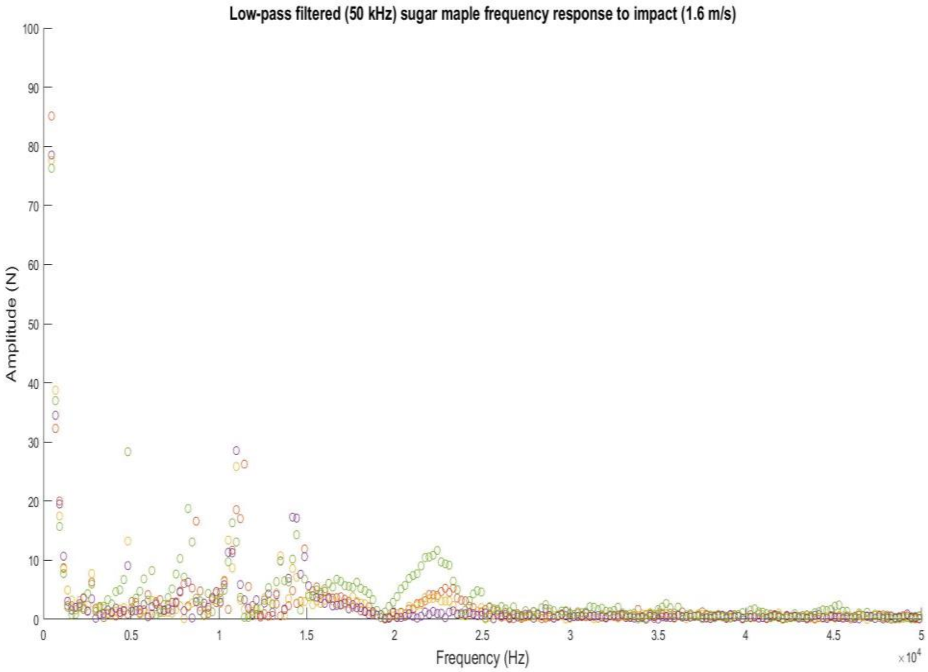

**Figure 24. (cont.)** Low-pass filtered frequency response of tree species impacted in the CEAST 9350 (in alphabetical order). Samples of dimensions 20x20x20 mm, impact velocity 1.6 m/s, and impact energy of 2.9 J. Samples exhibited tight frequency distribution around ~ 5, 10, 15 kHz with greater amplitudes of ~ 20-30 kHz.

**F**

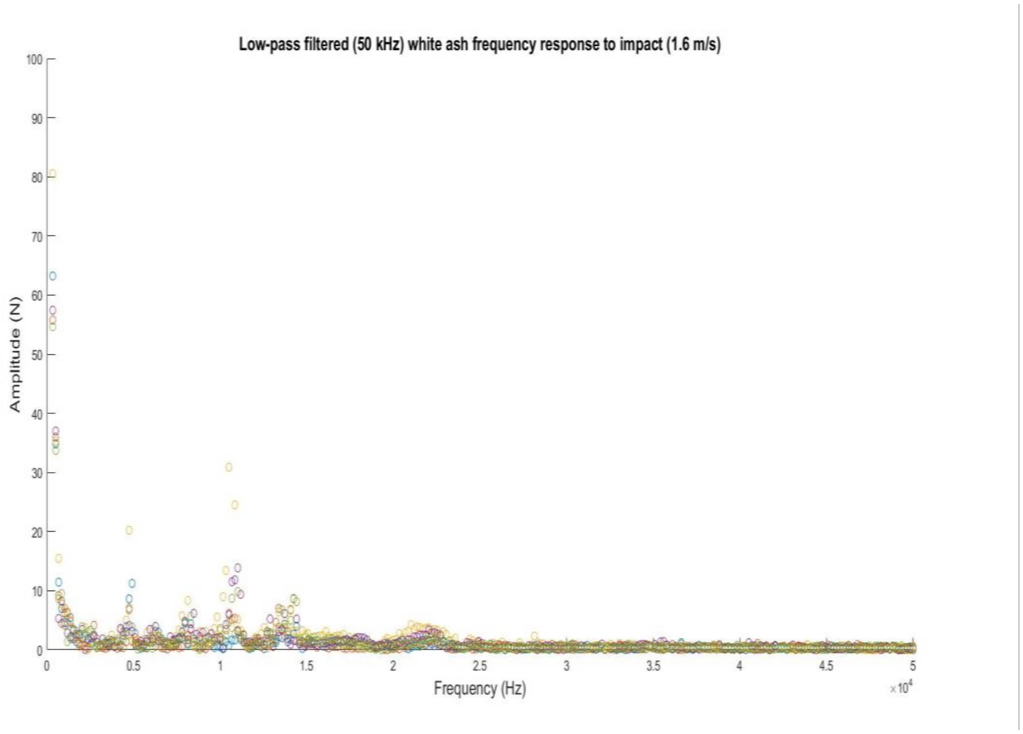

**Figure 24. (cont.)** Low-pass filtered frequency response of tree species impacted in the CEAST 9350 (in alphabetical order). Samples of dimensions 20x20x20 mm, impact velocity 1.6 m/s, and impact energy of 2.9 J. Like pecan, oscillation frequencies were concentrated around ~ 5, 10, and 14 kHz.

**G**

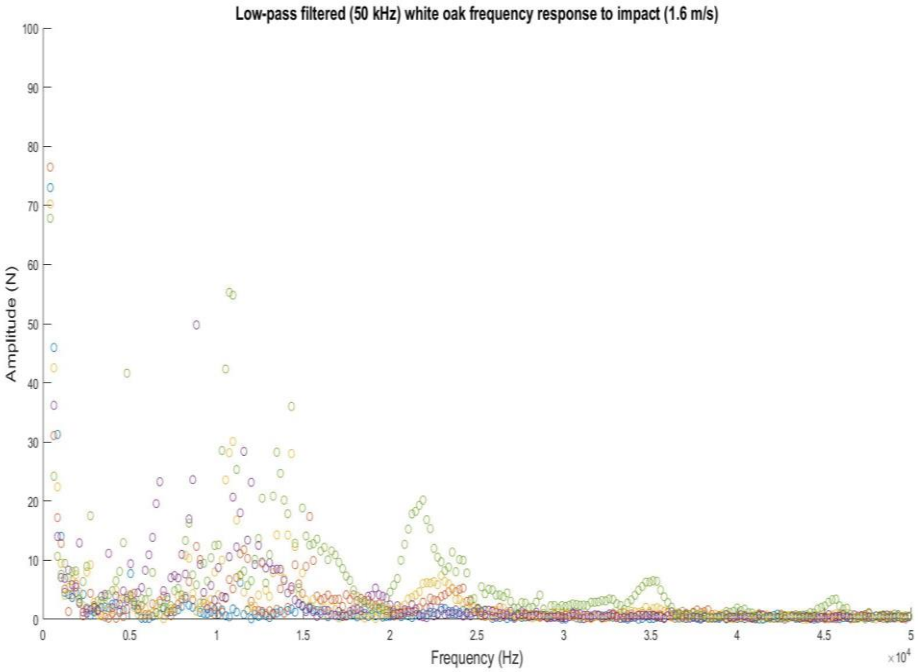

**Figure 24. (cont.)** Low-pass filtered frequency response of tree species impacted in the CEAST 9350 (in alphabetical order). Samples of dimensions 20x20x20 mm, impact velocity 1.6 m/s, and impact energy of 2.9 J. White oak exhibited a large range of broad signals, all of high amplitude between ~ 20-55 N.

**H**

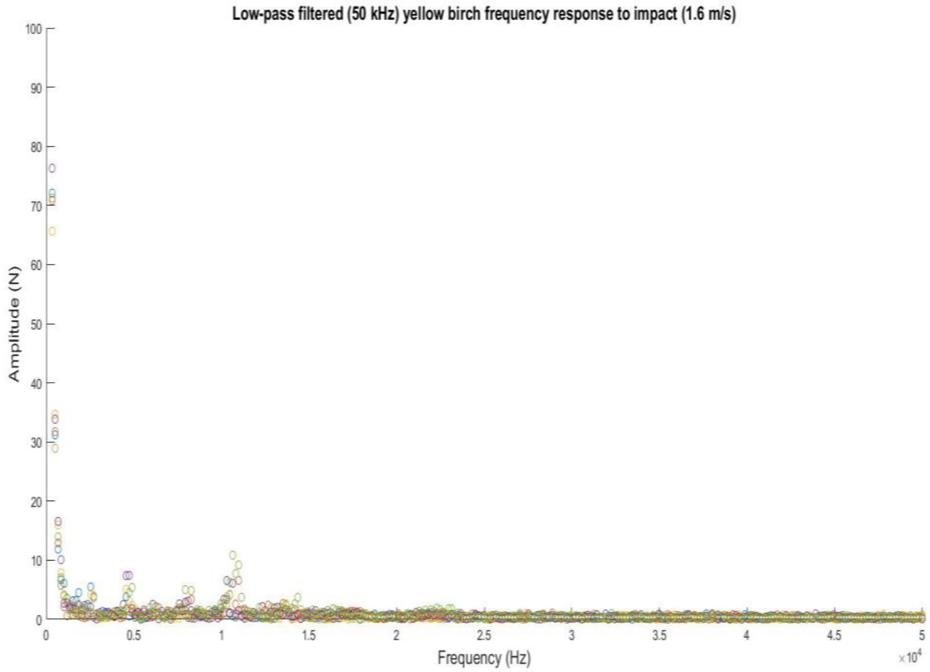

**Figure 24. (cont.)** Low-pass filtered frequency response of tree species impacted in the CEAST 9350 (in alphabetical order). Samples of dimensions 20x20x20 mm, impact velocity 1.6 m/s, and impact energy of 2.9 J. Tight frequencies distributions at ~ 5, 10 kHz below 10 N characterized the response indicating strong damage absorption.

**I**

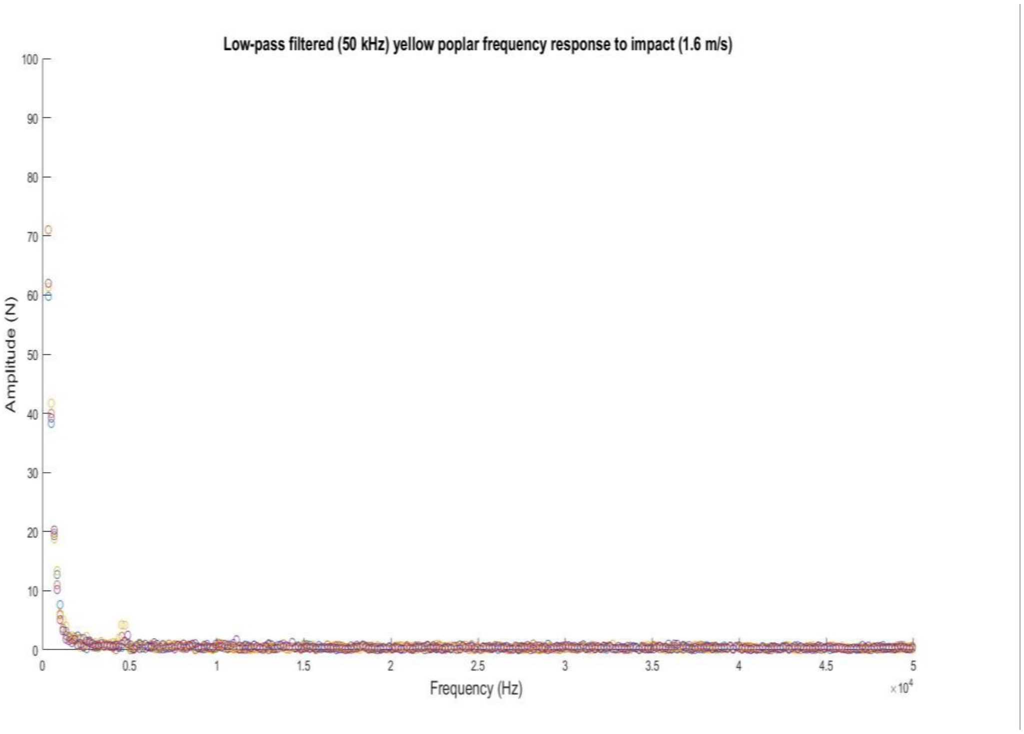

**Figure 24. (cont.)** Low-pass filtered frequency response of tree species impacted in the CEAST 9350 (in alphabetical order). Samples of dimensions 20x20x20 mm, impact velocity 1.6 m/s, and impact energy of 2.9 J. A single frequency response of ~ 5 kHz with a low amplitude of ~5 N indicates minimum mechanical reverberations in the sample.

Lower peak forces coincided with greater penetration depth and lower deceleration, analogous to how the crumple zone of a car disperses energy from a collision. African mahogany exhibited notable results: in addition to being the most impact resistant wood species identified in the custom drop-tower testing (energy of failure = 42 kJ/m$^2$), it maintained a low average peak force of 580 N and high displacement of 6.1 mm (Figure 23, A). The data also show a lower amplitude of oscillations (maximum of 10 N) tightly grouped at ~5000 and ~11000 Hz relative to other tested tree species (Figure 24, A). Black walnut, the second most impact resistant species identified (energy of failure = 35 kJ/m$^2$), behaved similarly with a low average peak force (640 N), moderate displacement (4.9 mm) (Figure 23, B), and low oscillation amplitude ( < 10 N)

(Figure 24, B). Compared to African mahogany the black walnut exhibited a greater range of frequencies in between samples. Pecan specimens exhibited high reverberations at the initial moment of impact and high average peak forces of 1000 N (Figure 23, C),. Additionally, frequency decomposition found multiple oscillations of > 20 N amplitude at ~5000, ~10000, and ~15000 Hz (Figure 24, C),. This response of high initial reverberations, high average peak force, and large amplitude oscillations was shared by the other two ring porous tree species of white ash and white oak (Figure 23, F and G. Figure 24, F and G). Despite diffuse porous sugar maple's different microstructure and higher energy of failure (29 $kJ/m^2$), it shared many similar responses with the ring porous species. It absorbed the dynamic load primarily through its stiffness as indicated by its higher peak force (1000 N) and lower displacement (4.5 mm) (Figure 23, E),. A noticeably higher amplitude of material reverberation ( > 30 N) is also apparent at multiple frequencies (~5000, ~10000, ~15000 Hz), particularly during the initial contact (Figure 24, E),. Yellow birch and yellow poplar exhibited slightly lower peak forces of 890 and 930 N, respectively, and were characterized by reverberations of lower magnitude (Figure 23, H and I. Figure 24, H and I). Red alder exhibited the lowest peak force and greatest penetration depth which is consistent with its low density (Figure 23, D. Figure 24, D).

To understand the initial discontinuities observed in the ring porous species and sugar maple it is important to list the three factors affecting the CEAST 9350's data collection: inertial effects due to the probe and specimen mass, mechanical bending loads of the test specimen, and test system ringing due to a combination of the device, probe, and specimen. Because the discontinuities do not persist in similar amplitude after the first millisecond of impact and are observed only in certain species, test system ringing is unlikely to have caused them [54]. Inertial effects (load exerted on the impactor tip by specimen acceleration from rest) tend to dominate within the first 20 μs of impact and are implausible given the relatively impact velocity and long timescale of the oscillations which persist for at least 200 μs [55]. Mechanical responses are the most plausible explanation and could indicate either (1) a high degree of sequential breaking or (2) a more rigid body response in the ring porous specimens and maple. Evidence of the former was visible in the response of white ash to impact (Figure 19) and may explain the oscillations in ring porous species, though the mechanism remains unclear for maple.

**Table 11.** Summary of CEAST 9350 drop-tower test results

| **Vessel distribution** | **Tree Species** | **Peak force [N]** | **Penetration depth [mm]** | **Peak deceleration [G]** | **Oscillation frequencies [kHz]** |
|---|---|---|---|---|---|
| Diffuse porous | *Red alder* | 420 ± 140 | 7.6 ± 3.3 | -17 ± 6.5 | Broad response |
| | *African mahogany* | 580 ± 80 | 6.1 ± 0.29 | -25 ± 3.4 | 5, 11 |
| | *Yellow birch* | 890 ± 39 | 5.1 ± 0.20 | -38 ± 1.9 | 5, 10 |
| | *Yellow poplar* | 930 ± 74 | 5.2 ± 0.30 | -40 ± 3.6 | 5 |
| | *Sugar maple* | 1000 ± 34 | 4.5 ± 0.15 | -43 ± 1.3 | 5, 10, 15 |
| Semi-diffuse porous | *Black walnut* | 640 ± 64 | 4.9 ± 0.63 | -27 ± 3.0 | 5, 15 |
| Ring porous | *Pecan* | 1000 ± 52 | 4.5 ± 0.40 | -44 ± 2.4 | 5, 10, 15 |
| | *White ash* | 1000 ± 35 | 5.1 ± 0.27 | -44 ± 1.5 | 5, 10, 14 |
| | *White oak* | 1300 ± 220 | 3.9 ± 0.62 | -65 ± 23 | Broad response |

Other questions remain as to the mechanism of the unique responses by each species, however. African mahogany and black walnut, for example, maintained low peak forces and decelerations despite their high density. While red alder's low density makes intuitive sense as an explanation for its time-displacement behavior it provides no details as to its mechanisms. To understand these differences, a closer examination of the damage is necessary.

## 5.3 SEM results and microstructure

African mahogany, black walnut, red alder, white ash, and white oak were examined post-impact using scanning electron microscopy to better understand damage mechanisms (Figure 25-29).

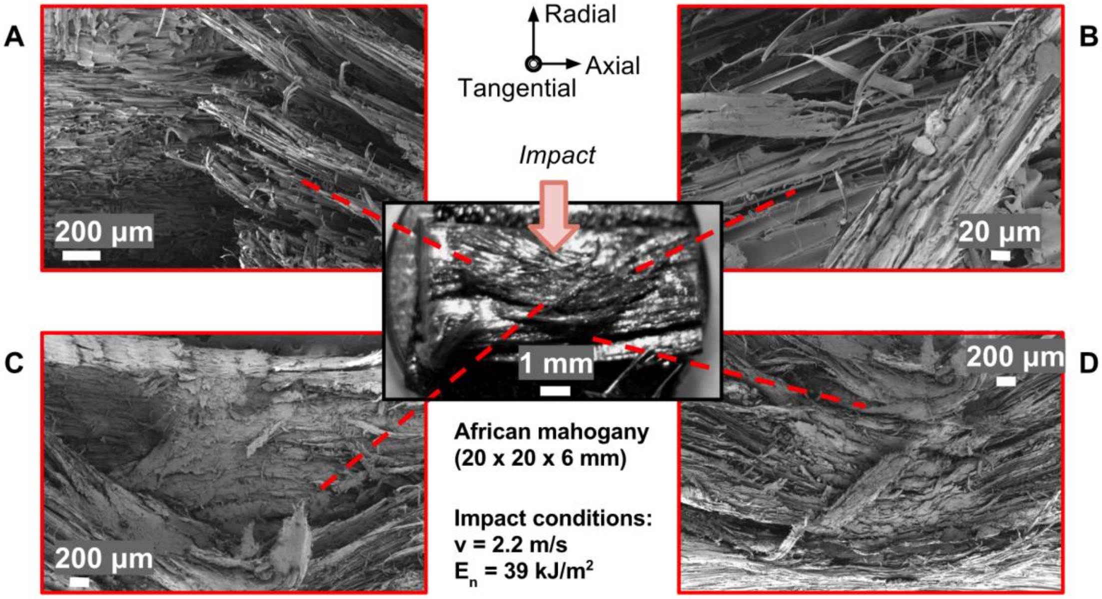

**Figure 25.** Tangential face of African mahogany sample fragment after impact. (A) Fiber tear out, (B) tracheid unraveling, and (D) fiber bending are visible on closer inspection.

African mahogany appeared to absorb the impact by a combination of fiber pullout and fiber bending. Examining the ends of the torn tracheids (Figure 25, A & B) revealed a combination of cell wall delamination and unwinding of the cell walls, indicating damage in the P/ML and S layers (Figure 5), respectively. The section of tracheids directly impacted exhibited a separation from adjacent fibers (Figure 25, C) allowing entire segments of tracheids to bend (Figure 25, D) rather than deform or fail locally.

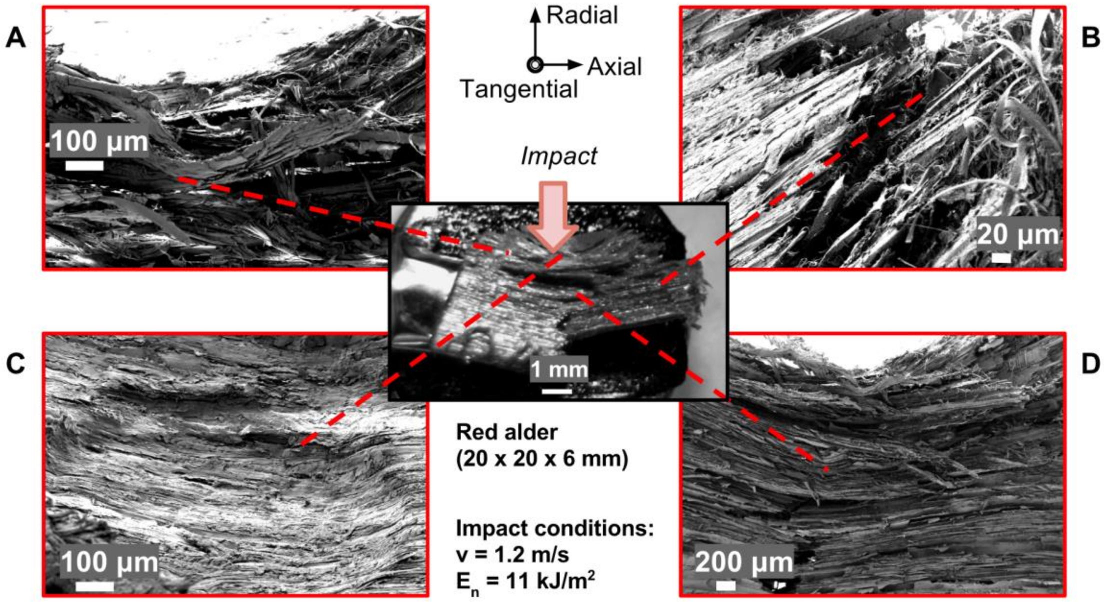

**Figure 26.** Tangential face of red alder sample fragment after impact. (A) Fiber tear out, (B) tracheid unraveling, and (C) fiber bending and (D) breaking are visible.

Red alder displayed remarkably similar failure mechanisms to African mahogany: extensive fiber pullout (Figure 26, A) and tracheid unraveling (Figure 26, B) are clearly observed in addition to marked fiber bending (Figure 26, C & D). Unlike in African mahogany the tracheids directly below the impact site fractured past their limit of deformation, likely due to their lower density.

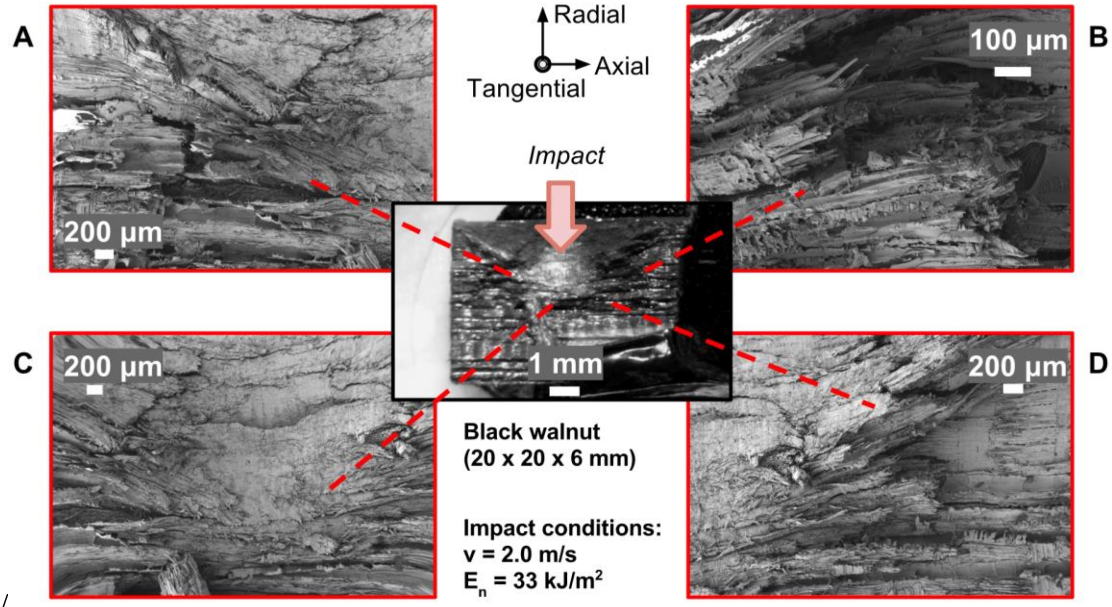

/

**Figure 27.** Tangential face of black walnut sample fragment after impact. (A) Tracheid fracture and (B, D) bending were observed. (C) Cracks are visible throughout the sample.

In black walnut the impact caused tracheids to break off into large pieces and limited the degree of bending as a damage absorption mechanism. Examining the ends of these fragments shows little unraveling of the tracheid cell walls with some tracheid tear out (Figure 27, A and B). The fragmentation of tracheids and lack of cell wall unwinding indicate fewer shearing and tensile mechanisms that would resist impact compared to African mahogany, as evident in the fractures seen in Figure 27, C and D.

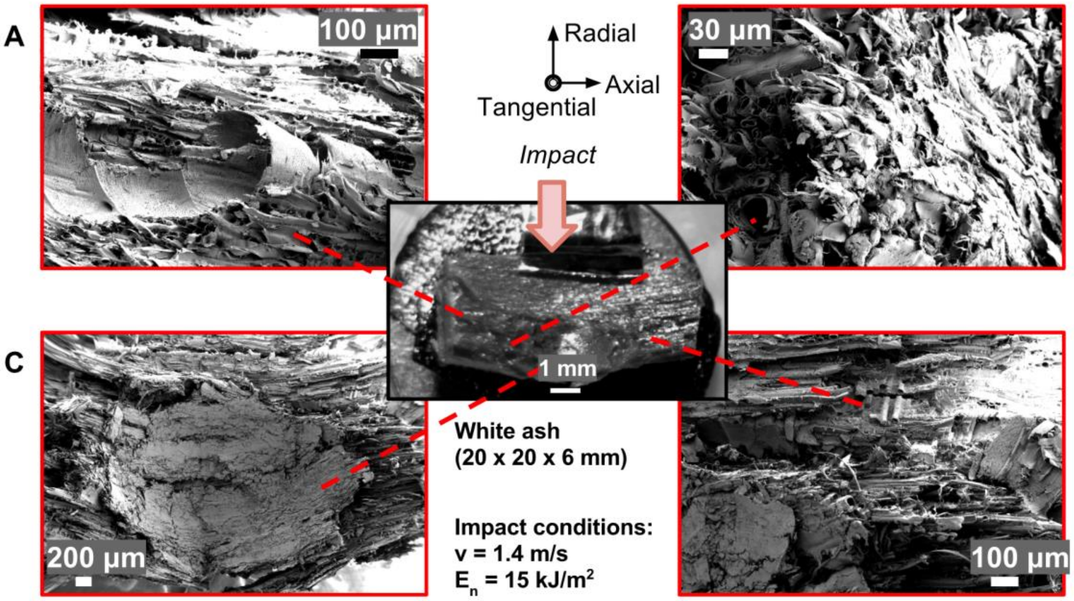

**Figure 28.** Tangential face of white ash sample fragment after impact. The ends of the broken tracheids appear cleanly fractured (A, B). Impact generated a highly rough surface on the cleaved face (C, D), with little to no fiber pull out visible.

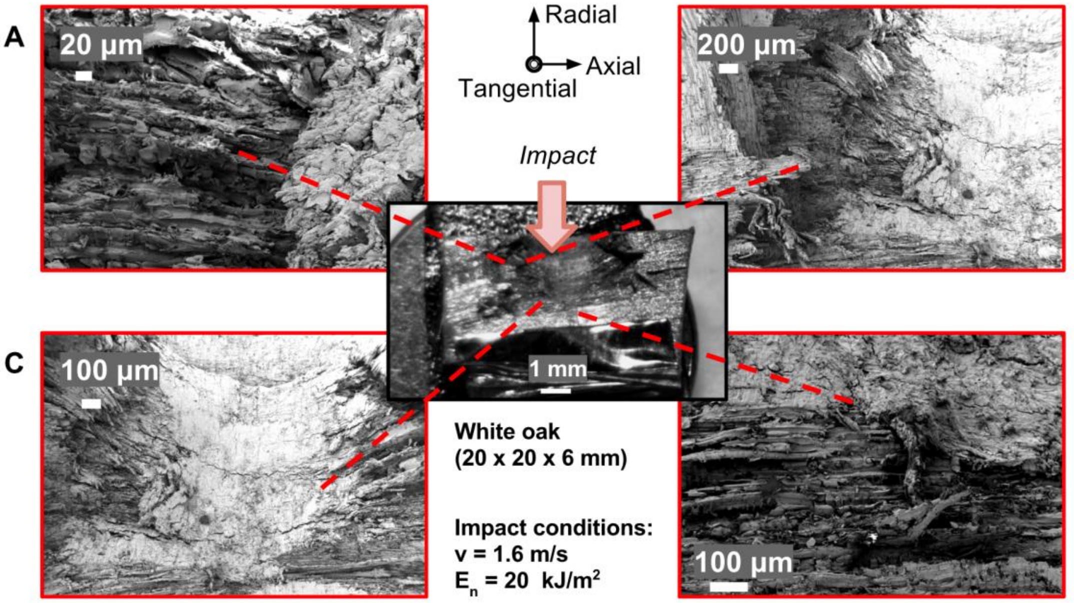

**Figure 29.** Tangential face of white oak sample fragment after impact. Impact generated (A) little to no fiber pull out and (B, C) a highly rough surface on the cleaved face. The ends of the broken tracheids appear cleanly fractured (A, D). No fiber bending is observed, even in the tracheids adjacent to the densification zone left by the impact (D).

In white ash and white oak, the tracheids appear to contribute very little in the way of tensile resistance to fracture. The samples appear highly fragmented with an uneven surface, and the tracheids appear only fractured but largely unbent. Broken tracheid ends show no signs of unwinding and the mode of failure appears to be highly brittle.

These different failure mechanisms between African mahogany and red alder, black walnut, and white ash and white oak can be understood in the context of fiber-reinforced composite failure, a critical factor in which is the level of adhesion between the fibers and matrix. At high levels of adhesion brittle failure occurs in the composite with little energy absorption, while at low levels of adhesion multiple delaminations occur simultaneously without significant fiber failure. At an optimal degree of adhesion delamination occurs sequentially: an advancing crack delaminates a fiber, loads the fiber in tension until failure, and then delaminates the subsequent fiber to repeat the process. This mechanism (progressive delamination) allows well designed fiber-reinforced composites to absorb large amounts of impact energy [56]. White ash and white oak show telltale signs of high adhesion failure with little fiber pullout and indications of brittle tracheid fracture. This is concordant with their high peak forces, indicating that these species primarily absorbed impact through high fracture initiation energy but had few mechanisms to prevent propagation. In addition to the sequential breaking mechanism it is likely that these species had a rigid body response contributing to the large osciallations described in the previous section. Black walnut showed similar signs, but fewer cracks to indicate some improved shock dampening mechanisms in the wood. African mahogany and red alder on the other hand showed extensive signs of tensile damage and deformation in the tracheids. These results suggest that despite the low peak forces observed in the CEAST 9350 for African mahogany and red alder, these species possess high crack propagation energy. This optimal adhesion may be further enhanced by the additional damage absorption mechanism of tracheid unwinding observed in the two species.

In summary, vessel distribution and fiber adhesion were found to influence damage mechanisms in radial impact loading in the manners summarized in Table 12 and 13, respectively:

**Table 12.** The effects of vessel distribution on failure in radial impact

| **Vessel distribution** | **Species** | **Characteristics of failure in radial impact** | |
|---|---|---|---|
| | | *Macroscopic* | *Microscopic* |
| Ring porous | *Pecan, white ash, white oak* | Rupturing, delamination at vessel layers, splitting. Increased density did not improve impact resistance. | RT crack propagation through vessels, peeling TR crack propagation. |
| Diffuse porous | *African mahogany, red alder, sugar maple, yellow birch, yellow poplar* | Splitting. Increased density improved impact resistance. | Peeling TR crack propagation. |

**Table 13.** The effects of fiber adhesion on failure in radial impact

| **Adhesion** | **Species** | **Characteristics of failure in radial impact** | |
|---|---|---|---|
| | | *Macroscopic* | *Microscopic* |
| Over-adhered | *White ash, white oak* | Low penetration depth, high peak force, high oscillations | Brittle failure of tracheids, cohesive failure |
| Optimally adhered | *African mahogany, black walnut, red alder* | High penetration depth, low peak force, low oscillations, fiber pullout | Tracheid bending and unwinding, progressive delamination |

# 6 Applications and Bio-inspiration

Despite millennia of use, wood may have yet more to teach us. The study of density and structure dependent strain rate sensitivity may be broadened to even more commercial species of lumber. Species of trees especially suitable for dynamic loading may be identified for construction in earthquake-prone regions—conversely, tree species historically used in earthquake-prone regions may be worth studying to translate accumulated cultural knowledge into scientific understanding. It is likely that as the volume of the wood deployed increases according to application even more hierarchical mechanisms may be identified.

Wood may inspire the design of future materials, too, via bio-inspiration (the study of natural materials structures for engineering applications). The three key characteristics of impact resistant wood identified in this work were: (1) a uniform distribution of pores to yield optimal density efficiency, (2) an interlocking grain structure to divert cracks into winding patterns, and (3) an optimal degree of adhesion between fibers to produce progressive delamination. These principles can be combined in future work: interlocking grain can be replicated in Bouligand-like structures in 3D-printing. Such structures have already been fabricated by Grunenfelder et al. [57], but a hierarchical porosity of fine honeycombs and large tubules mimicking tracheids and vessels, respectively, can be introduced to maximize weight efficiency. Another possibility is to re-create tracheids by winding fiber-composite laminates into tubes, and arranging those tubes into larger honeycomb structures to create weight-efficient materials. With proper adhesion it may be possible to introduce unwinding mechanisms of impact dissipation observed in African mahogany and red alder. This mechanism, combined with interlocking-grain like structures, will enhance the shock absorption allowed by progressive delamination.

# 7 Conclusion

This thesis explores the relation between wood structure and mechanical properties in low velocity impact conditions in African mahogany, (*Khaya ivorensis*), black walnut (*Juglans nigra)*, pecan (*Carya illinoinensis*), red alder (*Alnus rubra*), sugar maple (*Acer saccharum*), white ash (*Fraxinus americana*), white oak (*Quercus alba*), yellow birch (*Betula alleghaniensis*), and yellow poplar (*Liriondendron tulipifera*). Southern live oak (*Quercus virginiana*) was also examined but due to its lower moisture content (8% rather than 12%) conclusions could not be drawn from that species. Drop-tower testing revealed that unlike in quasi-static conditions, the density is an inaccurate predictor of mechanical properties (work to fracture) in dynamic conditions. Using analysis of variance (ANOVA) it was shown that in a general linear model the vessel distribution strongly interacted with density in predicting the normalized work to failure in impact. No such relation was observed in quasi-static conditions. In the CEAST 9350 drop-tower it was observed that lower peak forces coincided with greater penetration depth and lower deceleration, with no clear relation to density or vessel distribution.

Damaged samples examined using scanning electron microscopy (SEM) revealed that adhesion may play a strong role in the load-time response in impact. Wood species able to absorb large amounts of energy and maintain low peak forces showed several mechanisms of damage absorption indicative including tracheid unwinding, tracheid bending, and tracheid breaking—the progressive damage is similar to the progressive delamination observed in the failure of optimally adhered fiber-reinforced composites. The major findings in this thesis are:

- Drop-tower testing on a custom-built instrument at 1:5 scale was used to perform low velocity ( < 3 m/s) impact tests on wood specimens. Plotting the normalized impact energy of failure against the density of samples revealed different relationships depending on the vessel distribution.
    - While increasing density improved the impact resistance of diffuse porous trees (vessels uniformly distributed), ring porous trees (vessels distributed in narrow circumferential bands with each growth ring) showed no such improvement.
    - Statistical analysis indicated density alone had little effect on impact resistance but interacted strongly with vessel distribution. In comparison to previously studied biological materials, some wood species (black walnut, sugar maple, and African mahogany) were shown to be as impact resistant as hydrated ram horn (energy of failure = 32 $kJ/m^2$) and surpassing others (armadillo scutes, abalone nacre, bovine femur) while being less dense than all of the above examples.
- Quasi-static (0.2 mm/s) compressive testing performed with geometry identical to the custom drop-tower confirmed literature results that density is an excellent predictor of wood quasi-static mechanical behavior. Vessel distribution had no discernable effect on the work to failure.
    - Comparing SEM images of impacted and quasi-statically compressed ring porous ash revealed different modes of failure. Whereas quasi-statically compressed samples were characterized by vessel collapse propagating from the loading face, impacted specimens exhibited crack propagation into vessel bands and little vessel deformation.

  - The concentration of vessels in tangential bands characteristic of ring-porous wood created intrinsic weakness in impact due to compressive and shearing forces on the vessel causing RT crack propagation and large failure events in the vessel regions.
- Drop-tower testing to non-failure on the CEAST 9350 revealed load-time data indicative of how different species absorbed impact. Species such as sugar maple and black walnut that had similar impact energies of failure (~32 kJ/m$^2$) in the custom drop-tower were shown to behave in varying ways.
  - Most species exhibited low penetration depth, high deceleration, and high peak forces (~1000 N) with strong reverberations, indicating a stiff material response.
  - Other species (African mahogany, black walnut, and red alder) absorbed the impact while maintaining low peak forces below ~600 N and reverberations via greater penetration depth, analogous to how the crumple zone of a car softens a collision.
- SEM of damaged samples revealed possible mechanisms of shock dissipation in wood species able to maintain low peak forces including tracheid bending over large lengths, tracheid breaking, and tracheid unwinding.
  - Species that tended to exhibit high peak forces and strong reverberations showed highly localized tracheid densification, little tracheid bending, and large amounts of cracks and fractures. The damage modes characteristic of low and high peak forces resembled those of optimally adhered and overly adhered fiber-reinforced composites, respectively.

  - Low peak force samples exhibited signs of progressive tracheid damage similar to progressive delamination, and high peak forces samples exhibited signs of simultaneous brittle failure similar to that in overly adhered composites.
- African mahogany exhibited the most notable results: in addition to being the most impact resistant wood species identified in the custom drop-tower testing (energy of failure = 42 $kJ/m^2$), it maintained a low average peak force of 580 N and high displacement of 6.1 mm. The data also show a lower amplitude of oscillation relative to other tested tree species indicating low flexural vibration. In failure it also exhibited wavy fracture surfaces which were only observed in species with interlocking grain. A wide variety of impact dissipating mechanisms were observed in this species.

Revisiting the thesis hypothesis, it was found that the distribution of vessels in wood species heavily influenced their impact resistance in radial loading conditions. Wood species of uniform vessel distribution (diffuse porous) showed improved energy of failure with increasing density whereas wood species with vessels confined to circumferential bands corresponding to spring/summer growth (ring porous) showed no improvement. Interlocking grain in African mahogany (energy of failure = 42 $kJ/m^2$) caused diverted crack paths indicating possible advantages over typical straight-grain wood in absorbing impact. Finally, adhesion between tracheids heavily influenced failure modes—similar to optimally adhered fiber-reinforced composites, wood species such as African mahogany and red alder were able to fail in progressive cycles of tracheid delamination from adjacent fibers and tracheid failure, maintaining low peak forces.

## 7.1 Recommendations for Future Research

This work is limited in scope of the number of species examined, loading conditions, and application of derived principles. Future work includes:

- Micromechanical studies of tracheid adhesion forces between different species across varying strain rates
- Micromechanical studies of tracheid unwinding forces across varying strain rates
- Finite element modeling of various wood anatomies and topological optimization to derive further engineering principles for impact resistant cellular solids
- Biomimicry attempts to test the vessel distribution hypothesis
- Biomimicry attempts to replicate the hierarchical damage absorption of tracheid progressive delamination and tracheid unwinding

# Appendix

## Appendix A. Polishing Protocol

1. Embed samples in epoxy and leave overnight.
2. Cut samples to suitable cross-sections using a saw.
3. Using medium grit sandpaper (1200 grit) on a rotating lap, smooth the edges of the sample so that there are no ridges on the sample and so that the sides are square with each other and opposite surfaces are parallel. This is so that your sample will lie flat when being imaged.
4. After using the lap, rinse sample in DI water and use compressed air to blow off grit or particles.
5. Using a finer grit sand paper (2400 grit), sand the sample back and forth in one direction. Use a microscope to check that all of the large scratches have been sanded away. Rinse sample with DI water and put into sonicator for 5 minutes to remove excess particles. Use compressed air to dry.
6. Using 3µm aluminum oxide polishing liquid and the corresponding polishing pad, Polish sample perpendicular to the direction from the last step. Once you see no scratches in the previously sanded direction, sonicate for another 5 minutes to remove excess particles.
7. Use the 0.05µm diamond polishing media with the corresponding polishing pad to polish samples. Polish in circular directions until scratches from the previous step have disappeared. Sonicate sample for 5 minutes and dry with compressed air.

# References

[1] S. E. Naleway *et al.*, “Structural Design Elements in Biological Materials : Application to Bioinspiration Structural Design Elements in Biological Materials : Application to Bioinspiration,” no. August, 2015.

[2] D. Showalter, “Ovis canadensis, bighorn sheep,” *David Showalter Nature Photography*, 2014. .

[3] R. L. Caldwell, “Odontodactylus scyllarus, mantis shrimp,” *Wikipedia*, 2004. .

[4] J. Slama, “Dryocopus pileatus, pileated woodpecker,” *Audobon Society*, 2009. .

[5] Unknown, “Equus ferus caballus, Mongolian horse,” *Three Pulpa Wallpaper Facets*. .

[6] L. J. Gibson and M. F. Ashby, *Cellular Solids: Structure & Properties, 2nd edition*. Cambridge: Cambridge University Press, 1999.

[7] “USS Constitution: The Legend Restored,” *All Hands*. [Online]. Available: http://www.navy.mil/ah_online/constitution/.

[8] “Louisville Slugger bat,” *Glam Slam--Where Fashion Meets Sports*, 2017. .

[9] Atirador, “RPD-44 Russian light machine gun,” *Wikipedia*, 2008. .

[10] “Bowling alley flooring,” *Tiki Lanes Bowling*. .

[11] “DH-98 Mosquito bomber,” *Wikipedia*. .

[12] “Mayans and Aztecs at War,” *History on the Net*, 2014. .

[13] “Battle of Salamis.” [Online]. Available: https://s-media-cache-ak0.pinimg.com/originals/bf/47/29/bf47290d9a319ad8f63f99fee4960d1e.jpg
.

[14] “Viking round shield,” *The Viking Rune*. [Online]. Available: http://www.vikingrune.com/2012/01/viking-shield/.

[15] D. W. Green, J. E. Winandy, and D. E. Kretschmann, “Mechanical properties of wood fiber,” *Tappi J.*, 1959.

[16] M. F. Ashby, “The Fracture and Toughness of Woods,” *Proc. R. Soc. A*, no. 398, pp. 261–280, 1985.

[17] P. Greil, T. Lifka, and A. Kaindl, “Biomorphic Cellular Silicon Carbide Ceramics from Wood,” *J. Eur. Ceram. Soc.*, vol. 18, pp. 1961–1973, 1998.

[18] “Softwood microstructure,” *Queensland Timber Merchant*, 2015. .

[19] E. Meier, “Roupala montana, leopardwood,” *Wood Database*. .

[20] E. Meier, “Fraxinus Americana, white ash,” *Wood Database*. .

[21] E. Meier, “Acer Saccharum, sugar maple,” *Wood Database*. .

[22] E. Meier, “Carya Cordiformis, bitternut hickory,” *Wood Database*. .

[23] A. C. Wiedenhoeft, “Chapter 3 - Structure and Function of Wood Contents,” *Wood Handb. - Wood as an Eng. Mater.*, pp. 1–18, 2010.

[24] F. Barthelat, Z. Yin, and M. Buehler, “Structure and mechanics of interfaces in biological materials.”

[25] C. Zollfrank and J. Fromm, “Ultrastructural development of the softwood cell wall during pyrolysis,” *Holzforschung*, vol. 63, no. 2, pp. 248–253, 2009.

[26] R. J. Astley, K. A. Stol, and J. J. Harrington, “Modelling the elastic properties Part Ih The cellular microstructure.”

[27] R. Thomas, *Wood Technology*. Raleigh, NC: North Carolina State University, 1977.

[28] J. R. Griffiths and V. R. Salanitri, “The strength of spider silk,” *J. Mater. Sci.*, vol. 15, no. 2, pp. 491–496, 1980.

[29] J. McKittrick, P. Y. Chen, S. G. Bodde, W. Yang, E. E. Novitskaya, and M. A. Meyers, “The structure, functions, and mechanical properties of keratin,” *Jom*, vol. 64, no. 4, pp. 449–468, 2012.

[30] “Aluminum 6061-T6,” *ASM Aerospace Specification Metals Inc.* [Online]. Available: http://asm.matweb.com/search/SpecificMaterial.asp?bassnum=ma6061t6.

[31] H. E. Desch and J. M. Dinwoodie, *Timber, its Structure and Properties*, 6th ed. London: Macmillian Education, 1981.

[32] I. Cave, “The anisotropic elasticity of the plant cell-wall,” *Wood Sci. Technol.*, vol. 2, pp. 268–278, 1968.

[33] I. Cave, “The longitudinal Young’s modulus of Pinus Radiata,” *Wood Sci. Technol.*, vol. 3, pp. 40–48, 1969.

[34] "Specific stiffness - specific strength," *University of Cambridge Dept. of Engineering*, 2002. .

[35] G. Jeronimidis, "The Fracture Behaviour of Wood and the Relations between Toughness and Morphology," *Proc. R. Soc. London. Ser. B, Biol. Sci.*, vol. 208, no. 1173, pp. 447–460, 1980.

[36] M. . Ashby, "The properties of foams and lattices," *Philos. Trans. R. Soc. A Math. Phys. Eng. Sci.*, vol. 364, no. 1838, pp. 15–30, 2006.

[37] A. T. Price, "Mathematical discussion on structure of wood in relation to its elastic properties," *Philos. Trans. R. Soc. A Math. Phys. Eng. Sci.*, vol. 228, pp. 1–10, 1928.

[38] P. Srinavasn, "Elastic and Thermal Properties of Timber," *J. Indian Inst. Sci.*, vol. 23, pp. 223–253, 1940.

[39] L. W. Wood, "Relation of strength of wood to duration of load," *For. Prod. Lab. Serv. U. S. Dep. Agric.*, vol. R1916, p. 10, 1951.

[40] A. Elmendorf, "Stresses in impact," *J. Franklin Inst.*, vol. 182, no. 6, pp. 771–790, 1916.

[41] C. G. Gilbertson, M. Asce, and W. M. Bulleit, "Load Duration Effects in Wood at High Strain Rates."

[42] A. J. M. Leijten, "Impact crash and simulation of timber beams," *Comput. Eng.*, vol. 30, pp. 859–868, 2001.

[43] S. R. Reid and C. Peng, "Dynamic uniaxial crushing of wood," *Int. J. Impact Eng.*, vol. 19, no. 5–6, pp. 531–570, 1997.

[44] J. J. Harrigan, S. R. Reid, and C. Peng, "Inertia effects in impact energy absorbing materials and structures," *Int. J. Impact Eng.*, vol. 22, no. 9–10, pp. 955–979, 1999.

[45] S. Lee *et al.*, "Impact testing of structural biological materials," *Mater. Sci. Eng. C*, 2011.

[46] D. Cassens, "Purdue extension Controlling Moisture Content in Stored Lumber," West Lafayette, IN.

[47] A. D7136, "Standard Test Method for Measuring the Damage Resistance of a Fiber-Reinforced Polymer Matrix Composite to a Drop-Weight Impact Event," *Analysis*, vol. i, pp. 1–16, 2005.

[48] D. Bernier, "Maple, ash, or birch? Which wood is best for a baseball bat, and why.," *Pro Baseball Insider*. .

[49] R. Hernandez, "Review of 2009 MLB Baseball bat regulations," *RockBats, LLC*, 2009. .

[50] “The Live Oak Story,” *National Park Service*, 2016. [Online]. Available: https://www.nps.gov/guis/learn/historyculture/the-live-oak-story.htm.

[51] M. Obregon, “The macuahuitl: an innovative weapon of the Late Post-Classic in Mesoamerica,” *Arms Armour*, vol. 3, no. 2, pp. 127–148, 2006.

[52] U. Forest Service and F. Products Laboratory, “Wood Handbook, Wood as an Engineering Material,” 2010.

[53] “Wood Technology Transfer Fact Sheet: Khaya ivorensis.,” *USDA Forest Service*. .

[54] “Standard Test Method for High Speed Puncture Properties of Plastics Using Load and Displacement Sensors 1.”

[55] T. S. Desisto, “ASTM special technical publication 563 INSTRUMENTED IMPACT TESTING,” Philadelphia, PA, 1973.

[56] P. K. Mallick, *Fiber-Reinforced Composites*, 3rd ed. Boca Raton, FL: Taylor & Francis Group, 2008.

[57] L. K. Grunenfelder *et al.*, “Bio-inspired impact-resistant composites,” in *Acta Biomaterialia*, 2014.